UNIVERSITÀ DEGLI STUDI DI PADOVA

Dipartimento di Fisica e Astronomia "Galileo Galilei"

Master Degree in Astrophysics and Cosmology

Final dissertation

Development of a lepto-hadronic model of the high-energy emission of Active Galactic Nuclei

Thesis supervisor

Prof. Elisa Bernardini

Thesis co-supervisor

Dr. Cosimo Nigro

Candidate

Dimitrios K. Maniadakis

Academic Year 2022/2023

Abstract

Cosmic rays are high-energy particles that arrive at Earth with energies that can reach up to 10^{20} eV. Their acceleration sites remain a mystery, but multi-messenger astrophysics aims to solve this puzzle by combining information from different "messengers" from all four fundamental forces of nature. Among these messengers, neutrinos play a crucial role in understanding the acceleration sites of cosmic rays, as they are produced in hadronic emission processes. Blazars are one of the main candidates of cosmic ray acceleration. Especially after the multi-messenger observation of an astrophysical neutrino associated with a flaring blazar in 2017, the modelling of the spectral energy distribution of blazars using both leptonic and hadronic emission processes is crucial to understand the physical processes taking place in the jets of blazars. In this thesis, I extend the capabilities of the python package `agnpy`, which was designed for modeling the high-energy emission of jetted active galactic nuclei using only leptonic models. Specifically, I implement two of the most significant hadronic processes that occur in the jet: the proton synchrotron radiation and the photo-meson production, with the latter being the primary source of neutrino emission in blazars. As of today, `agnpy` will be the first open-source code to include the mentioned hadronic emission processes for modeling the high-energy emission of jetted active galactic nuclei.

Contents

List of Figures

List of Tables

CHAPTER 1

Introduction

Cosmic rays are highly energetic particles that constantly bombard the Earth's atmosphere. The discovery of cosmic radiation in 1912 by Victor Hess led to the study of its properties, revealing that its intensity varied with geomagnetic latitude. It was only later, through the use of telescopes and experimental methods, that the true nature of the radiation was understood to be particles rather than electromagnetic radiation. They became crucial to high-energy astrophysics, as a significant amount of energy is often transmitted through these particles. They arrive at the earth with energies that can reach up to 10^{20} eV, with Larmor radii larger than the radius of our galaxy, indicating an extra-galactic origin. Nonetheless, the nature of the acceleration sites of these particles remains a mystery.

Multi-messenger astrophysics is a relatively new branch that tries to solve that puzzle. It attempts to combine information from different "messengers" from all four fundamental forces of nature and by doing so, to understand in more depth astrophysical phenomena. Neutrinos, the messenger of the weak force, are particularly important in the context of acceleration sites of cosmic rays. They are produced in the collision of a cosmic ray with a dense target or with their interaction with low energy photons. Hence, their detection could give important clues about the acceleration sites of cosmic rays. On September 22, 2017, a high energy neutrino was detected and associated with the source TXS 0506+056, a type of source that is considered one of the prime candidates for the

acceleration site of cosmic rays, a blazar.

Blazars are a subclass of active galactic nuclei with a relativistic jet pointing towards the observer's line of sight. While it is widely accepted that relativistic electrons are present in the jet, the existence of relativistic hadrons is still under debate. The modelling of the spectral energy distribution of blazars was mostly done with leptonic emission processes, where the high energy radiation is attributed to relativistic electrons scattering lower energy photons into higher energies. However, the multi-messenger observation of an astrophysical neutrino associated with a flaring blazar in 2017 has strengthened the argument for the presence of relativistic hadrons in the blazar jet. This discovery has led to renewed efforts to model the spectral energy distribution of blazars with both leptonic and hadronic emission processes in order to better understand the physical processes taking place in these objects.

The aim of this thesis is to develop a code capable of modelling the non-thermal emission of jetted active galactic nuclei using both leptonic and hadronic emission processes. It begins by introducing the concept of active galactic nuclei and blazars, their classification and the modelling of their spectral energy distribution using both leptonic and hadronic processes. Then, the `agnpy` package is presented, an open-source software designed for modelling the high-energy emission of jetted active galactic nuclei using just leptonic models. The main focus of the thesis is the implementation into `agnpy`, of the two most significant hadronic processes that take place in the jet: the proton synchrotron radiation and the photomeson process, the latter of which is responsible for neutrino emission in blazars. The thesis concludes with a discussion of the results obtained and our conclusions. As today, `agnpy` will be the first open-source code that includes the aforementioned hadronic emission processes for modelling the high energy emission of jetted active galactic nuclei.

CHAPTER 2

The Modelling of Jetted Active Galactic Nuclei

An active galactic nucleus (AGN) refers to a galactic nucleus that exhibits any activity related to the accretion onto a supermassive black hole. In other words, when a black hole at the center of a galaxy is actively consuming material from its surroundings, the galaxy is classified as an active galaxy hosting an AGN. AGNs emit an enormous amount of radiation as a result of this accretion process, and the luminosity of this radiation often surpasses the brightness of the entire galaxy that surrounds it. There exist various types of AGNs, and each type exhibits a unique observational signature. These distinctions between AGNs can be explained by the unification scenario which will be discussed later in this chapter.

Around the central black hole, our current understanding suggest that the matter surrounding it forms an accretion disk that radiates thermal radiation through friction. In addition, a dusty torus surrounds the system, which obscures the radiation observed depending on the viewing angle of the observer. They also exhibit narrow and broad line regions, which are regions of ionized gas that emit narrow and broad emission lines, respectively.

However, some AGNs also exhibit two relativistic plasma outflows perpendicular to the accretion disk, known as jets. Even though our knowledge regarding their formation is limited, the observational evidence suggest that they are magnetically aligned and can

reach distances of millions of light years. They are the dominant source of high-energy emission of jetted AGNs, since relativistic particles moving along the jet are emitting non-thermal radiation.

2.1 Active Galactic Nuclei

Seyfert's discovery of several peculiar galaxies in the nearby universe listed in the historical Messier catalogs ([13]) led to the identification of the first active galactic nuclei. They were detected as nearby galaxies that showed a luminosity peak at their center, while their emission lines in their optical spectrum had unusual intensity ratios, in comparison to other galaxies. In addition, they were extremely broad with a full-width-half-maximum of the order of $10000\,\mathrm{km\,s^{-1}}$. These galaxies were called (Seyfert 1943 [14]) "Seyfert galaxies".

Few years later following the first release of radio astronomical sources catalogs, there was an increased focus on compact radio sources. Their faint optical counterpart showed high variability and thus they were called quasi-stellar objects or quasars. Subsequent measurements of their extremely high redshift (for instance, refer to Schmidt 1963 [15]) revealed that quasars are actually extragalactic objects possessing immense luminosities up to $10^{48}\,\mathrm{erg\,s^{-1}}$.

Naturally, the question arose as to how could these objects be so incredibly luminous. Their immense luminosity and the fact that they emit radiation across the electromagnetic spectrum, from radio to gamma-ray frequencies, could not be explained solely by thermonuclear reactions in stars, indicating the presence of another emission mechanism. The gravitational force appears to be the only power source capable of generating such intense brightness. It was speculated that a supermassive black hole (SMBH) could be responsible, emitting vast amounts of energy through friction and viscosity while consuming material in an accretion disk. This scenario indicates that when most of the material has been accreted by the SMBH, its emission drastically reduces until finally the nucleus stops emitting radiation. If that is true, then AGNs could represent a primordial state of the normal galaxies we observe.

Seyfert galaxies and quasars, originally identified as distinct objects, are now recognized as two types of AGNs. Seyfert galaxies are a class of low-luminosity nearby AGNs, while quasars are a type of high-luminosity AGNs that can outshine their host galaxies.

2.1.1 The structure of the AGNs

An AGN is characterized by a central SMBH that attracts material towards itself, forming an accretion disk that spirals around the hole due to its gravitational pull. Additionally, there are two distinct regions of clouds known as the Broad Line Region (BLR) and Narrow Line Region (NLR), which give rise to the spectral lines observed. The presence of an opaque dusty torus causes the absorption of some radiation emitted by the nucleus and the BLR, re-emitting it in the infrared (IR) band. Some AGNs also display two opposing jets of plasma, in which relativistic particles emit radiation up to the γ-ray band. The structure of an AGN is shown in Figure 2.1

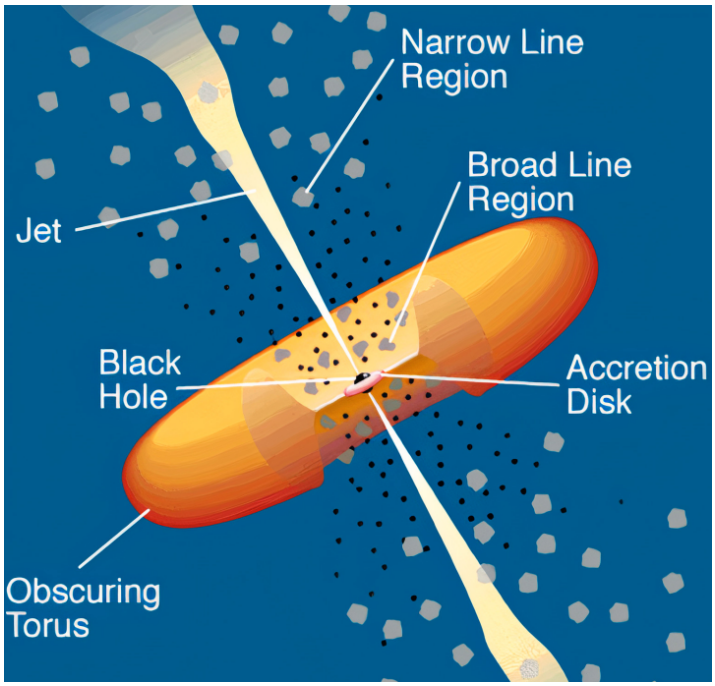

Figure 2.1: **The structure of an AGN**: In the center there is the Super Massive Black Hole while around it there is the accretion disk. The gray clouds shown are clouds of ionized plasma that form the Broad Line and Narrow Line regions. The large red *donut*-like structure around the black hole and the accretion disk is the dusty torus. Perpendicular to the plane of the accretion disk, there are the two jets of relativistic material [1].

Super Massive Black Hole

The accretion in an AGN is driven by the strong gravitational potential of the central SMBH. Its mass can be determined through various methods such as observing the motion of nearby stars and gas clouds and measuring the velocity dispersion of the host galaxy. Another method involves measuring the time delay between the brightness variations of the broad emission lines, which is known as reverberation mapping. The

mass can range from 10^6 up to 10^{10} solar masses.

Accretion disk

As already mentioned, the mechanism that produces the immense luminosity of the AGNs is believed to be accretion. Matter is anticipated to form a flattened structure known as an accretion disk as it spirals around the central black hole. The accretion disk is primarily composed of relatively cold material that emits blackbody radiation. As matter falls towards the black hole, its gravitational potential energy is converted into electromagnetic radiation, leading to the emission of intense radiation from the AGNs.

To estimate the energy radiated by a model accretion disk, we can assume that the gases in the accretion disk move in circular orbits due to their orbital velocity being much greater than their inward radial velocity. Then, to a good approximation, we can estimate the energy radiated by the disk neglecting the details of viscous forces acting within it. In addition, we can neglect the effect of gravity of the surrounding material, since it is very small compared to the SMBH. From Keplerian dynamics, the total energy of a mass m orbiting a gas is given by:

$$E = -G\frac{M_{\mathrm{BH}}m}{2r} \tag{2.1}$$

As the gas spirals inwards, it goes deeper into the potential well losing energy that maintains the disks temperature and is radiated in the form of black body radiation.

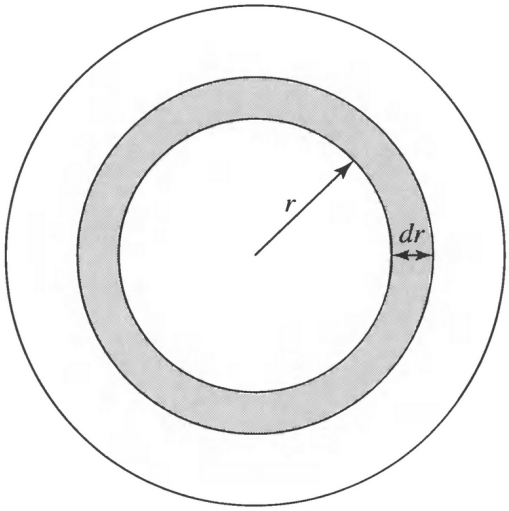

Figure 2.2: **Calculation of the luminosity of an accretion disk:** One of the (imaginary) annular rings constituting the accretion disk of an AGN [2].

Let us consider an annular ring depicted in Figure 2.2, with a width of dr and a radius of r, located inside the disk. Assuming a constant transfer rate of mass $\dot{m}$, the mass passing through the outer boundary of the circular ring in time t would be $\dot{m}t$. Since the disk is in a steady-state that doesn't change with time, no mass can accumulate within the ring. Hence, an equivalent amount of mass $\dot{m}t$ must also exit through the inner boundary of the ring in that time frame.

Conservation of energy requires that the energy radiated by the ring in time to be equal to the difference in the energy that passes through the ring's outer and inner boundaries:

$$dE = \frac{dE}{dr}dr = \frac{d}{dr}\left(-G\frac{M_{\rm BH}\,M}{2r}\right)dr = G\frac{M_{\rm BH}\dot{m}\,t}{2r^2}dr \tag{2.2}$$

where $M = \dot{m}t$ the orbiting mass entering and leaving the the ring. The energy dE radiated by the ring in time t is related to the luminosity dL by:

$$t\,dL = dE = G\frac{M_{\rm BH}\dot{m}t}{2r^2}dr \tag{2.3}$$

and by integrating this relation from R up to infinity, we find the disk's luminosity as [2]:

$$L_{\rm disk} = G\frac{M_{\rm BH}\,\dot{m}}{2R} \tag{2.4}$$

which is half of the total accretion luminosity. This relates to the Virial theorem, stating that half of the released potential energy is converted to kinetic energy while the other half then goes into terms that are not accounted for in the Virial theorem, which in this case would be radiation.

$$L_{\rm acc} = G\frac{M_{\rm BH}\,\dot{m}}{R}. \tag{2.5}$$

Although the gravitational force is the driving factor in accretion, radiation pressure also plays a crucial role. The presence of radiation creates a radiation pressure that acts against the gravitational force and pushes material away. As the accretion rate increases, the intensity of the radiation pressure also increases, eventually leading to a point where the two forces balance each other out. This balance is called the Eddington

limit, and it sets the maximum rate at which an object can accrete material before the radiation pressure overcomes the gravitational force. To calculate that, we consider the simple scenario of a steady spherically symmetric accretion flow into the black hole. Assuming that the gas consists of just hydrogen, the gravitational force that acts on each hydrogen atom is given by:

$$F_G = \frac{G\, M_{\rm BH}\, m_p}{r^2} \tag{2.6}$$

where we neglected the electron's mass since it is negligible compared to the mass of the proton. On the other hand, the radiative force is equal to:

$$F_{\rm RAD} = \frac{\sigma_T F}{c} = \frac{\sigma_T L}{4\pi r^2 c} \tag{2.7}$$

since $F = L/4\pi r^2$ is the apparent luminosity that the hydrogen "sees" and σ_T is the Thompson cross section. The Thompson cross section is proportional to the inverse square of the mass, therefore the radiative force is significantly smaller for protons. However, as the electrons gets accelerated by the radiative force, the Coulomb force attracts their respective protons towards them, causing the protons to move along with them. To calculate the Eddington limit, we set the gravitational force equal to the radiative force, as they balance each other out at this point:

$$\frac{G\, M_{\rm BH}\, m_p}{r^2} = \frac{\sigma_T L}{4\pi r^2 c}. \tag{2.8}$$

By solving for the luminosity, we obtain the Eddington luminosity as:

$$L_{\rm Edd} = \frac{4\pi c\, G M_{\rm BH} m_p}{\sigma_T} \cong 1.3 \times 10^{38} \frac{M}{M_\odot} \frac{\rm erg}{\rm s} \tag{2.9}$$

where $M_\odot$ is the solar mass.

Finally, we would like to mention the efficiency of the accretion mechanism energetically. The equations (2.3) and (2.4) were calculated in the approximation that R defines a hard surface. In the case of an accreting black hole however, it defines the radius of the event horizon and a significant fraction of the accretion energy may be lost into the black hole itself. The uncertainty in this case can be parameterised by the introduction of a dimensionless quantity η representing the efficiency of the accreting mechanism

([16]):

$$L_{\rm acc} = 2\,\eta\,GM_{\rm BH}\dot{m}/R_{\rm sch} = \eta\,\dot{m}\,c^2 \tag{2.10}$$

where $R_{\rm sch} = 2GM/c^2$ is the Schwarzschild radius of the black hole. The parameter η quantifies how efficiently the rest mass energy of the accreted material is converted into radiation, with a typical magnitude of approximately 0.1.

Broad and Narrow Line Regions

Within AGNs, there exist gas cloud regions surrounding the central core and accretion disk. These gas clouds receive constant illumination from the thermal radiation of the disk, leading to atomic transitions and line emission. The velocity of the gas cloud, which is dependent on its distance from the central black hole, determines the Doppler broadening of the emission lines. Regions closer to the black hole, at distances of 0.01 to 1 parsec, exhibit broader emission lines, named Broad Line Regions, which their Full Width at Half Maximum (FWHM) typically ranges from 10^3 to 10^4 $\mathrm{km\,s^{-1}}$. Instead, the regions further away, at distances greater than 300 parsec, demonstrate narrower emission lines, referred to as Narrow Line Regions, and typical values of the FWHM are 300 to 500 $\mathrm{km\,s^{-1}}$

Dust Torus

A torus of gas and dust surrounds the central region of an AGN, composed of optically thick dusty clouds. It absorbs the optical, UV, and soft X-ray radiation emitted from the accretion disk and the Broad Line Region. The amount of obscuration depends on the inclination of the observer's line of sight with respect to the normal to the disk, and a greater or lesser part of the emitted radiation can be intercepted. If the source is observed edge-on, the inner regions of the AGN are blocked by the torus, and the contribution from the absorbed radiation and the BLR are not visible in the spectrum. However, if the source is observed face-on, the BLR and the disk are not obscured, and the broad emission lines are present in the spectrum. In both cases, the contribution from the NLR (Narrow Line Region) is visible since it is placed outside of the torus. The radiation from the torus is mainly emitted in the infrared band.

Jets

We observe two perpendicular relativistic plasma outflows at approximately 10% of the AGN. Their existence remains a topic of intense debate due to our limited comprehen-

sion of these objects. According to our current understanding, these outflows arise from a combination of a poloidal magnetic field and a rotating black hole, which generate an electric field and a toroidal magnetic field. This produces an out-flowing poynting flux that is eventually created the jet which accelerates into relativistic speeds. These jets originate from a region close to the SMBH at about 1 parsec, but can extend to mega parsec scales.

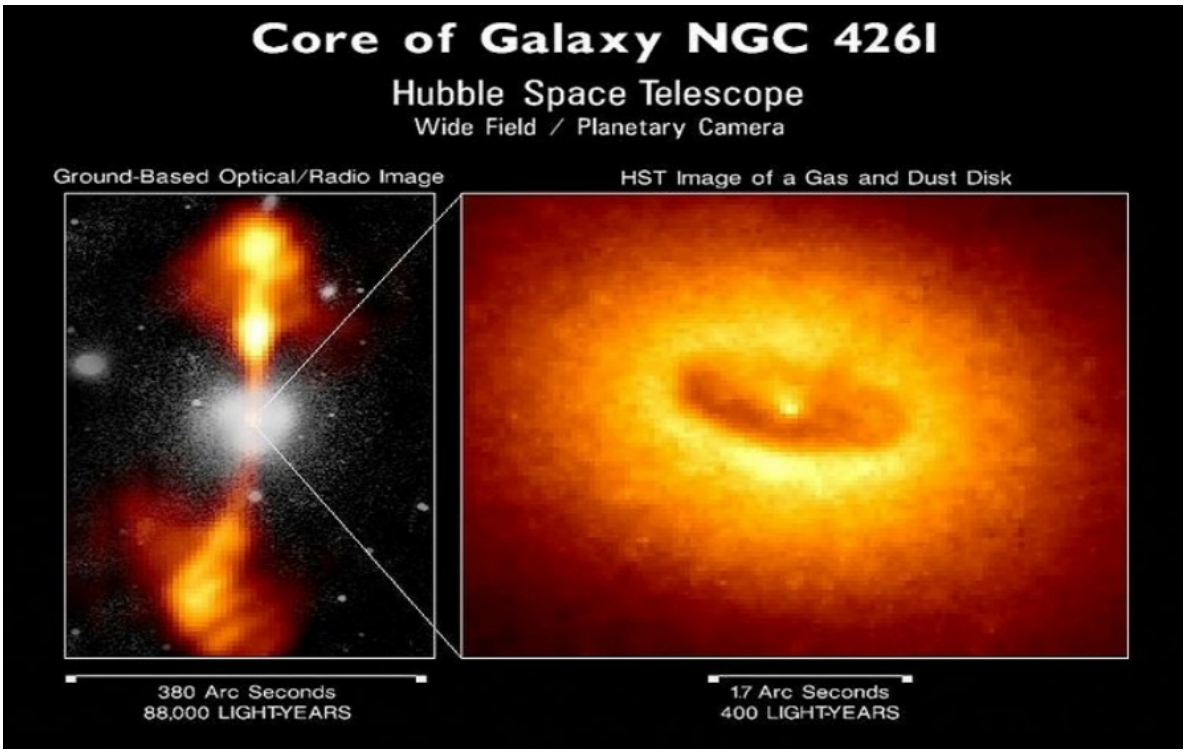

Figure 2.3: **The AGN NGC 4261:** On the left panel, it is an optical image of the galaxy where the relativistic jets are seen in radio in false-color, while on the right panel the dust torus and the obscuration of the accretion disk's radiation are shown. [3].

The jets are known for their ability to accelerate particles to extremely high energies, making them one of the most powerful particle accelerators in the universe. They emit non-thermal radiation across a broad range of energies, from radio waves to gamma rays. While there is strong evidence that electrons accelerating in the plasma within the jet cause this emission, the presence of protons is also a likely possibility and is of particular interest: if protons are indeed present, it could suggest the possibility of the emission of neutrinos as well.

2.1.2 The Unification Model of the AGNs

A unification model developed in the 1980s explains all the different observed types of AGNs as systems with a central supermassive black hole (SMBH) that accretes matter, forming an accretion disk. The presence of jets determines whether an AGN is radio-loud or radio-quiet. However, it should be noted that the dichotomy between radio-loud and radio-quiet AGNs is not fully explained or theoretically supported, and is a weak point in the theory.

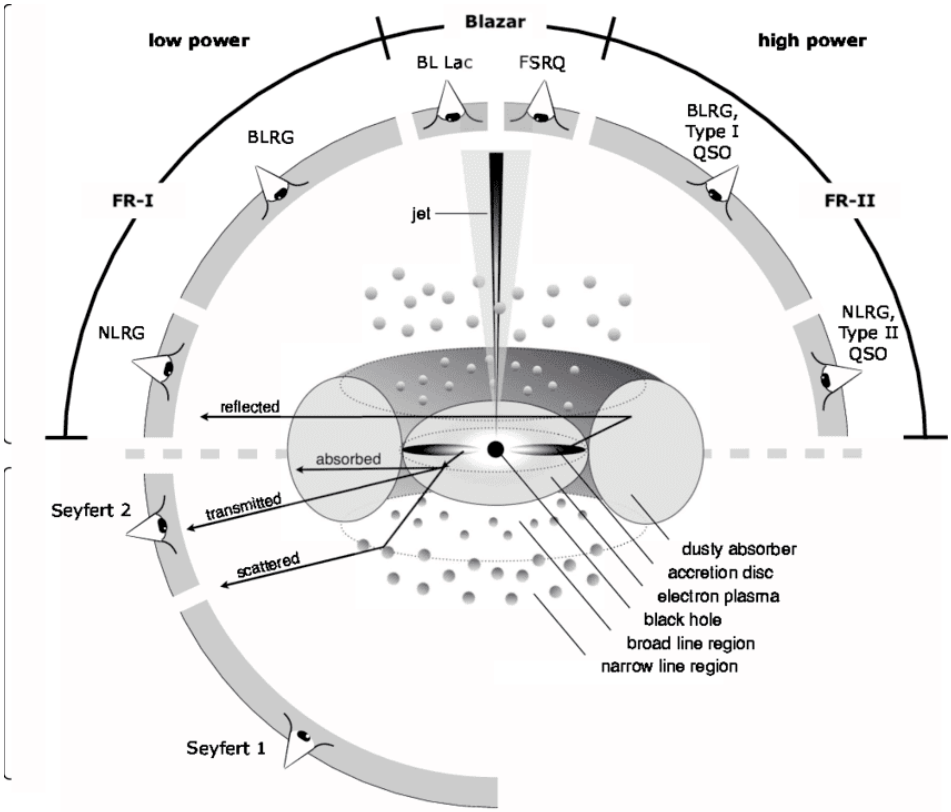

Figure 2.4: **The unified model of the AGNs**: The type of the AGN depends on the angle of observation and on the presence of the jet. There is a line which divides the scheme into two parts. The upper part shows the type of the AGN, depending on the observation angle, while a jet is present making all of them radio-loud. The lower part shows the radio-quite AGNs, since the jet is not present. [4].

The dust torus is a key component of the unification model. As we mentioned earlier, there are broad and narrow line regions in AGNs, which are clouds of gas. The broad line regions can be obscured by the dust torus, whereas the narrow line regions are outside of it. Depending on the angle of observation, we may only observe the NLR emission lines, since the emission of the BLRs is obscured by the torus. However, if we observe the AGN face-on, we can also detect the emission from the BLRs. This explains

the difference between Seyfert 1 and 2 galaxies based solely on orientation: Seyfert 1 galaxies have apparent broad line regions, whereas in Seyfert 2 galaxies, broad lines can only be observed in polarized light, suggesting that in this case, we are observing scattered radiation in the direction of the observer. Additionally, the direct observation of a dust torus, such as in the case of the nearby AGN NGC 4261 (Figure 2.3), provides strong evidence supporting this scenario. In Figure (2.4), a representation of the unified model is shown.

2.2 Blazars

Jetted AGNs whose relativistic jets are pointing exactly at the observer or very close at their line of sight, are called Blazars. Due to the geometry of blazars, their relativistic jets are closely aligned with the observer's line of sight. This alignment causes the intrinsic emission component to appear highly boosted in the observer's frame due to the relativistic Doppler effect, making their radiation to go to even higher energies.

They consist the most luminous AGN subclass, since their luminosity can reach up to 10^{48} erg s^{-1}. Their radiation is dominated by the non-thermal emission of accelerated particles, with a spectrum that ranges from radio to γ rays. Their Spectral Energy Distribution (SED) has a quite peculiar form, being comprised of two bumps, the low energy one that ranges from radio to X-rays and the high-energy one peaking in γ rays and reaching up to TeV energies in some extreme cases. Their radiation is highly variable, making them the most variable AGN subclass as well. In fact, the rapid flux variability observed in the highest energy bands, sometimes changing even within a few minutes, can help us probe the location of the emission region in the jet.

2.2.1 Classification of blazars

There are two main sub-classes of blazars: the BL Lac objects and the Flat Spectrum Radio Quasars (FSRQ). The classification criterion (Angel & Stockman 1980 [17]) regards the presence or absence of the emission line in the optical spectrum. If the equivalent width of the lines is greater than 5Å, the source is categorized as a FSRQ. Conversely, if the optical spectrum is a continuum, the source is classified as a BL Lac. The typical spectrum of FSRQs is shown in Figure 2.5, while the typical spectrum of BL Lacs is shown in Figure 2.6.

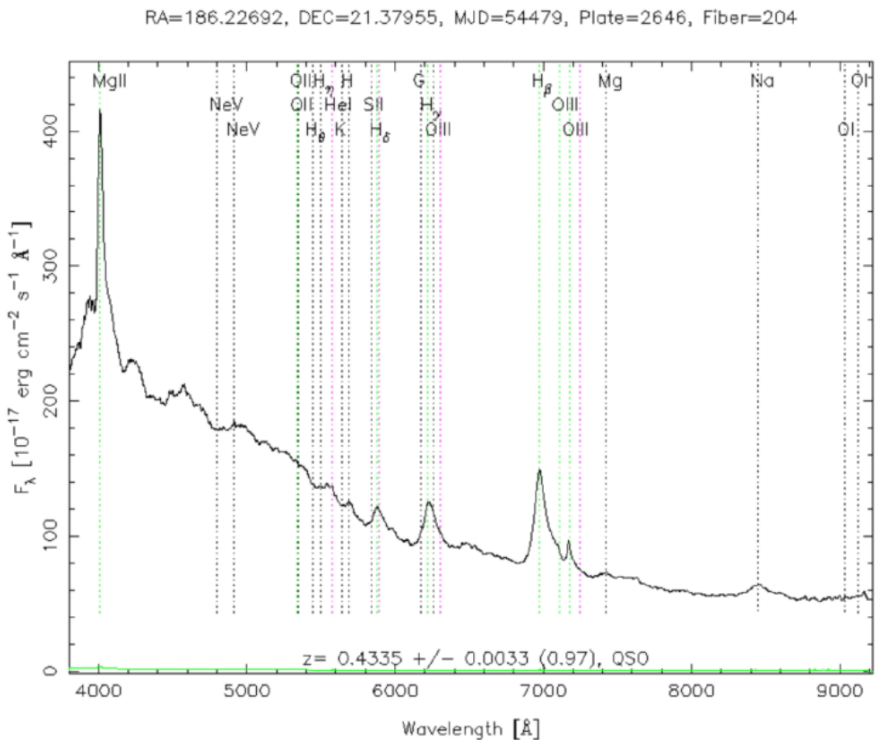

Figure 2.5: **The optical spectrum comparison of a FSRQ**: The spectrum has strong emission lines that identify the blazar as a Flat Spectrum Radio Quasar [5].

Their optical spectrum is not the only different between these two sub-classes. The luminosity function is different, where in the case of FSQRs is much brighter than that of the BL Lac objects (Padovani 1992 [18]). This can be attributed to the unification model which suggests that the brighter FSRQs are the FR II (from Fanaroff & Riley 1974 [19]) radio galaxies, dominated by distant hotspots in the jet, while the less intense BL Lac objects are the FR I galaxies, dominated by the core. Essentially, the difference in luminosity between the two types of galaxies is a result of their distinct jet structures.

Their redshift distribution (for a definition of redshift, refer to 2.2.3) is different as well. BL Lac objects have redshifts generally smaller ($z < 0.6$) than the FSQRs ($z \sim 1$). The absence of emission lines in the spectra of the BL Lac objects complicates the determination of the redshift. Therefore, it is possible that this difference in their redshift distribution is a consequence of the incomplete redshift catalogs of BL Lac objects, rather than the result of a more meaningful factor.

A further classification of the BL Lac objects can be done, considering the peak of the first bump of their SED. High-frequency-peaked BL Lac objects (HBL) have their peak in UV/X-ray light, while Low-frequency-peaked BL Lac objects (LBL) have a peak in IR/visible light. There are also Intermediate-frequency-peaked BL Lac objects where

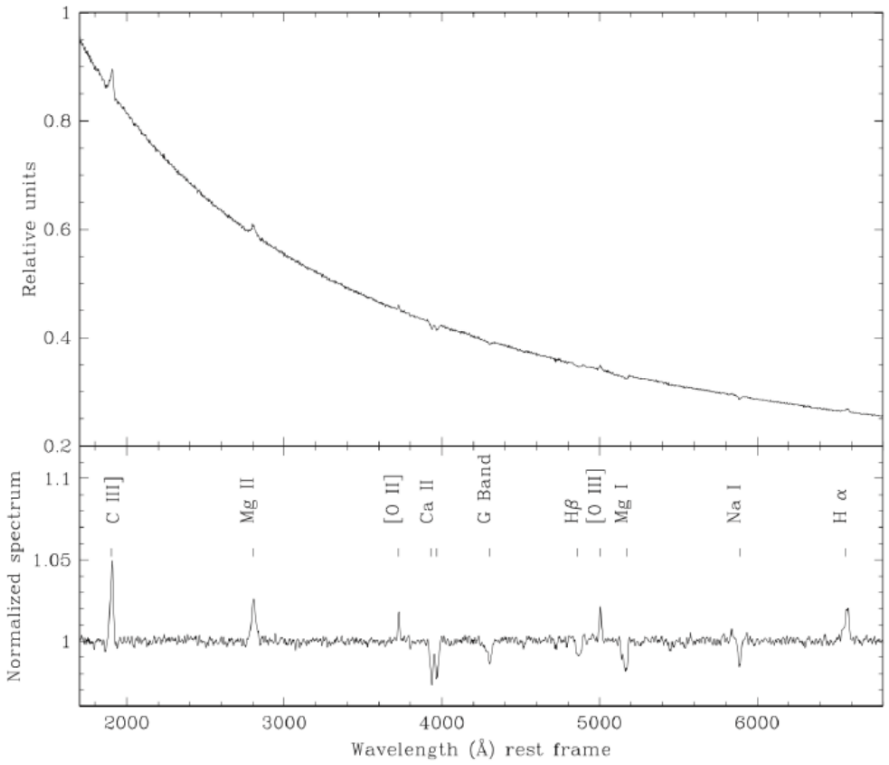

Figure 2.6: **The optical spectrum comparison of a BL Lac object:** the optical spectrum has very weak emission lines which identify the blazar as a BL Lac [6].

the peak is in the visible/UV range. An important observation is that as we move from BL Lac objects with higher peaks to those with lower peaks, we see an increase in luminosity. This suggests that the spectral energy distribution (SED) changes as a function of luminosity, the so-called blazar sequence (Fossati et al. 1998 [20], Ghisellini 2016 [21], Ghisellini et al. 2017 [7]) shown in Figure 2.7. FSRQs also fall within this sequence, specifically in the high luminosity range.

2.2.2 Relativistic effects: Relativistic beaming and the Relativistic Doppler effect

Since the radiation we detect from arises from an emission region within the jet that moves in relativistic velocities, the effects of relativity have to be taken into account. In fact, due to the relativistic Doppler effect, the luminosity observed is significantly higher than the true luminosity that would be measured in a frame moving alongside the emission region of the jet. Additionally, since all emission processes occur in the emission region's frame of reference but are observed from our frame on Earth, we need to perform appropriate relativistic transformations between these two frames when

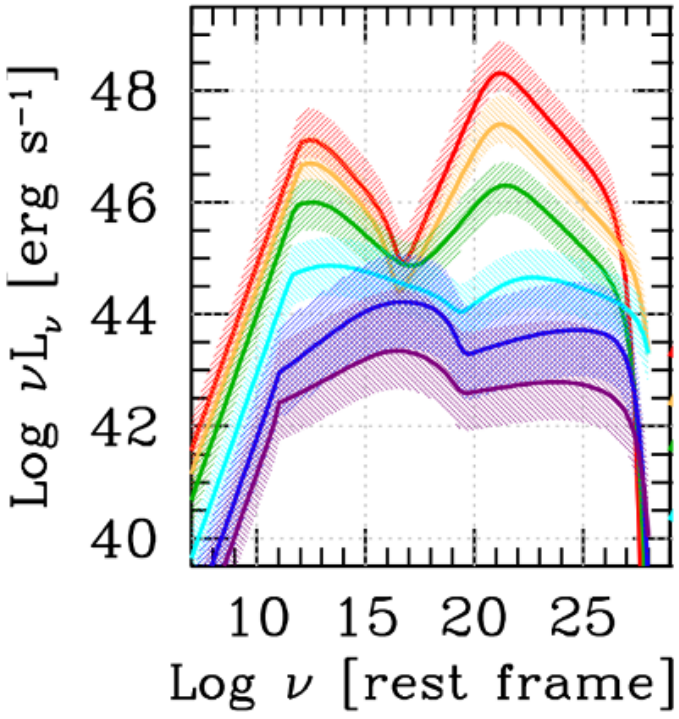

Figure 2.7: **The blazar sequence**: as we move from blazars where the peak of the low energy bump of their SED is in the higher energies, to those where the peak is in the lower energies, we see an increase in luminosity. The authors used data from the 3LAC catalog of γ-ray sources to create a sample of 747 objects, selected based on their γ-ray emission. They then divided the sources into γ-ray luminosity bins and calculated the average γ-ray luminosity as a function of redshift. [7].

calculating the spectra of these emission processes. A thorough understanding of the theory of relativity is essential for describing the physical processes within the jet and relativistic beaming. This sub-section is based on Dermer & Menon 2009 [8].

Relativistic transformations and four-vectors

In the framework of Special Relativity, the spacetime is flat and characterized by the spacetime interval, a relativistic invariant whose value remains constant regardless of the frame in which it is calculated:

$$\mathrm{d}s^2 = -c^2\mathrm{d}t^2 + \mathrm{d}x^2 + \mathrm{d}y^2 + \mathrm{d}z^2 \tag{2.11}$$

It is the length of a straight line between two events on the spacetime, and c is the speed of light, which is constant in any reference frame. Because of the constant speed of light, the value of the spacetime interval is zero for all frames of reference. Let

us consider two reference frames K and K', where the latter is moving with velocity $\vec{v} = v\,\hat{x}$ relative to the first (refer to Figure 2.8). The Lorentz transformations give the relations between these two reference frames, expressed as:

$$\begin{aligned} t' &= \Gamma(t - \beta x/c), \\ x' &= \Gamma(x - \beta ct), \\ y' &= y, \\ z' &= z. \end{aligned} \tag{2.12}$$

Where $\beta = v/c$ is the beta factor and $\Gamma = 1/\sqrt{1-\beta^2}$ the Lorentz factor. The inverse Lorentz transformations are given by:

$$\begin{aligned} t &= \Gamma\left(t' + \beta x'/c\right), \\ x &= \Gamma\left(x' + \beta ct\right), \\ y &= y', \\ z &= z'. \end{aligned} \tag{2.13}$$

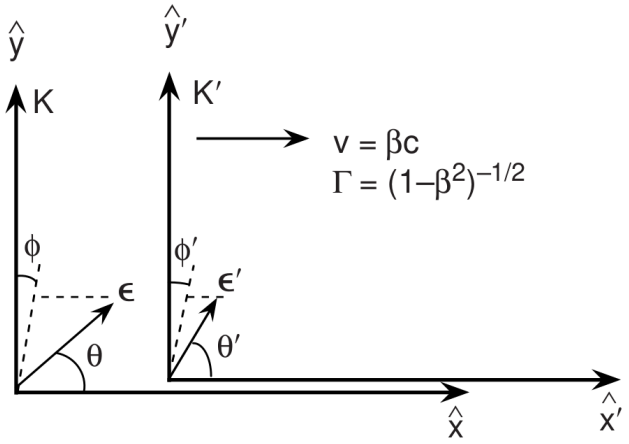

Figure 2.8: **Reference frames in Special Relativity:** Reference frame K' moving with speed $v = \beta c$ in the $\hat{x}$ direction with respect to frame K. A particle with energy ϵ in the K frame and ϵ' in the K' frame is shown. [8].

The time intervals in the two reference frames are different. It can be shown from equation (2.11) that:

$$dt = \Gamma dt' \tag{2.14}$$

We see that Γ is the Lorentz factor of the K' frame, as measured in the K frame. Similarly, if a particle is moving, it will have a Lorentz factor γ in the K frame and γ' in the K' frame. At this case, time dilation is $dt = \gamma dt'$.

In the context of special relativity, the momentum of a particle is equal to $\vec{p} = \gamma m \vec{u}$. However, quantities are expressed in the form of four-vectors. These vectors are defined in such a way that they transform based on the Lorentz transformations. The spacetime four-vector is $x^\mu = (ct, \vec{x}) = (x^0, x^1, x^2, x^3)$. All four-vectors transform according to:

$$\begin{aligned} x'^0 &= \Gamma \left(x^0 - \beta x^1 \right), \\ x'^1 &= \Gamma \left(x^1 - \beta x^0 \right), \\ x'^2 &= x^2, \\ x'^3 &= x^3. \end{aligned} \tag{2.15}$$

They can be constructed based on the spacetime four-vector and invariants that are unchanged under Lorentz transformations. The four-momentum of a particle with a Lorentz factor $\gamma = 1/\sqrt{1 - \beta_{\text{par}}^2}$ and beta factor $\vec{\beta}_{\text{par}} = \vec{u}/c$ is constructed as:

$$p^\mu = (\gamma mc, \gamma m \vec{u}) = \gamma mc \left(1, \vec{\beta}_{\text{par}} \right) = mc \left(\gamma, \vec{p}_{\text{par}} \right) \tag{2.16}$$

where $\vec{p}_{\text{par}} = \vec{\beta}_{\text{par}} \gamma$ is the dimensionless momentum. The time component of the four-momentum vector is equal to the energy of the particle over c, as the energy in special relativity is expressed as:

$$E = \gamma mc^2. \tag{2.17}$$

Since p^μ is a four-vector, it obeys the transformations given in (2.15), and therefore its components are expressed in the K' reference frame as:

$$\begin{aligned}
\gamma' &= \Gamma\left(\gamma - \beta p_x\right) = \Gamma\gamma\left(1 - \beta\beta_{\mathrm{par},x}\right), \\
p'_x &= \Gamma\left(p_x - \beta\gamma\right) \text{ or } \gamma'\beta'_{\mathrm{par},x} = \gamma\Gamma\left(\beta_{\mathrm{par},x} - \beta\right), \\
p'_y &= p_y, \\
p'_z &= p_z.
\end{aligned} \tag{2.18}$$

where the inverse transformations are obtained by interchanging the prime quantities and substituting $\beta \to -\beta$. As always, Γ represents the Lorentz factor and β indicates the beta factor of the K' frame, while γ represents the Lorentz factor and β_{par} indicates the beta factor of the particle, all as measured in the K frame. Similar to the Lorentz transformations which are derived from the spacetime invariant, the equations (2.18) are derived from the invariant expression:

$$E^2 = m^2c^4 + c^2p^2. \tag{2.19}$$

Relativistic beaming

In the case of light, the four-momentum is expressed as as:

$$k^\mu = \frac{\hbar}{m_e c^2}(\omega, c\vec{k}) \tag{2.20}$$

where $\vec{k}$ is the wave four-vector of the photon directed along the photon's direction of motion, with magnitude $2\pi/\lambda$ where λ is the wavelength of the photon. It can also be written, however, in the dimensionless form:

$$p^\mu = \epsilon\,(1, \frac{\hat{k}}{k}) \tag{2.21}$$

where $\epsilon = h\nu/m_e c^2$ is the dimensionless energy of the photon. The four-momentum of the photon undergoes a transformation based on the equations given in (2.15), like any four-vector. The Lorentz transformations can be expressed as:

$$\begin{aligned}
\epsilon' &= \Gamma(\epsilon - \beta\,\epsilon\,\frac{\hat{k}_x}{k}),\\
\epsilon'\,\frac{\hat{k'}_x}{k'} &= \Gamma(\epsilon\,\frac{\hat{k}_x}{k} - \beta\epsilon),\\
\epsilon'\,\frac{\hat{k'}_y}{k'} &= \epsilon\,\frac{\hat{k}_y}{k},\\
\epsilon'\,\frac{\hat{k'}_z}{k'} &= \epsilon\,\frac{\hat{k}_z}{k}
\end{aligned} \tag{2.22}$$

However, we can substitute the expressions of the $\vec{k}$ components in terms of the angles θ and ϕ:

$$\begin{aligned}
\epsilon' &= \Gamma\,\epsilon(1 - \beta\,\cos\theta),\\
\epsilon'\cos\theta' &= \Gamma\,\epsilon(\cos\theta - \beta),\\
\epsilon'\,\sin\theta' &= \epsilon\,\sin\theta,\\
\epsilon'\,\cos\phi' &= \epsilon\,\cos\phi
\end{aligned} \tag{2.23}$$

By substituting the first expression in to the other three, we get the equations:

$$\begin{aligned}
\cos\theta' &= \frac{\cos\theta - \beta}{1 - \beta\,\cos\theta},\\
\sin\theta' &= \frac{\sin\theta}{\Gamma(1 - \beta\,\cos\theta)},\\
\cos\phi' &= \frac{\cos\phi}{\Gamma(1 - \beta\,\cos\theta)}
\end{aligned} \tag{2.24}$$

which are the equations that describe the aberration of light in special relativity.

Let us now consider a photon being emitted in the K' reference frame and detected in K. If it is emitted at an angle $\theta' = \pi/2$ relative to the direction of motion, then $\cos\theta' = 0$ and therefore we get $\cos\theta = \beta$ from the first equation of (2.24). In the case of $\Gamma \gg 1$, then:

$$\beta = \sqrt{1 - \frac{1}{\Gamma^2}} \approx 1 - \frac{1}{2\Gamma^2} \approx 1 - \frac{\theta^2}{2} \tag{2.25}$$

where in the last step we just expanded $\cos\theta$, since $\beta = \cos\theta$. We see that the final result is:

$$\boxed{\theta \approx 1/\Gamma.} \tag{2.26}$$

Thus, all photons emitted in the forward direction in frame K' are concentrated within a narrow range of angles, where $\theta \lesssim 1/\Gamma$, when observed from frame K. This phenomenon is known as relativistic beaming (Figure 2.9).

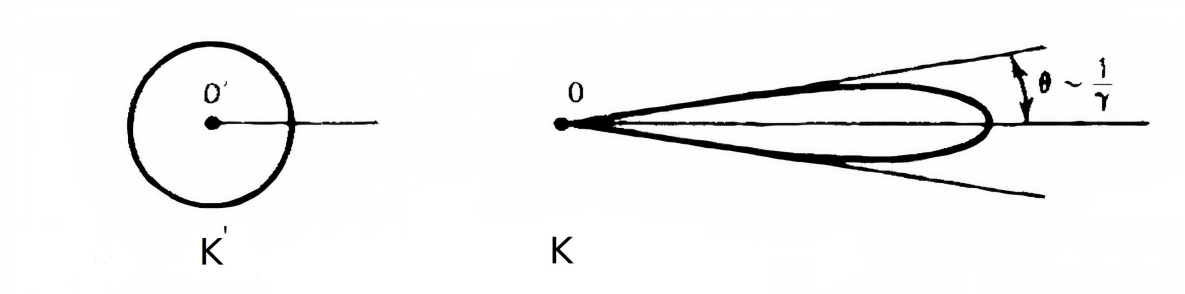

Figure 2.9: **Relativistic beaming**: In the emission frame K', the radiation is emitted isotropically, while in the observer's frame K, it is concentrated within a narrow range of angles $\theta \approx 1/\Gamma$ [9].

Relativistic Doppler effect

In the previous section, we derived the relation between the dimensionless energies in the K and K' frames (the first of equations (2.23)). The relativistic Doppler factor δ_D is then given by:

$$\frac{\epsilon}{\epsilon'} = \delta_{\rm D} \equiv [\Gamma(1-\beta\mu)]^{-1}. \tag{2.27}$$

In the case of relativistic beaming, we can approximate δ_D as:

$$\delta_{\rm D} \underset{\Gamma\gg 1,\theta\ll 1}{\longrightarrow} \frac{2\Gamma}{1+\Gamma^2\theta^2}. \tag{2.28}$$

However, it is useful to derive the relativistic Doppler factor in the case where an observer receives photons emitted at an angle θ with respect to the source's direction of motion, in the stationary reference frame K, as shown in Figure 2.10. After time Δt_* as measured in the reference frame K, the source's reference frame moves a distance:

$$\Delta x = \beta c \Delta t_* = \beta c \Gamma \Delta t' \tag{2.29}$$

where in the last step, we used the time dilation formula $\Delta t_* = \Gamma \Delta t'$. At time $t = t_*$ and location x, a light pulse is emitted. It is detected by the observer at time:

$$t = t_* + \frac{d}{c} - \frac{x \cos\theta}{c} \tag{2.30}$$

where d is the distance between the observer and the stationary reference frame K, as shown in Figure 2.10. The observer receives a second pulse of light emitted at a later time $t_* + \Delta t_*$, at time:

$$t + \Delta t = t_* + \Delta t_* + \frac{d}{c} - \frac{(x + \Delta x)\cos\theta}{c}. \tag{2.31}$$

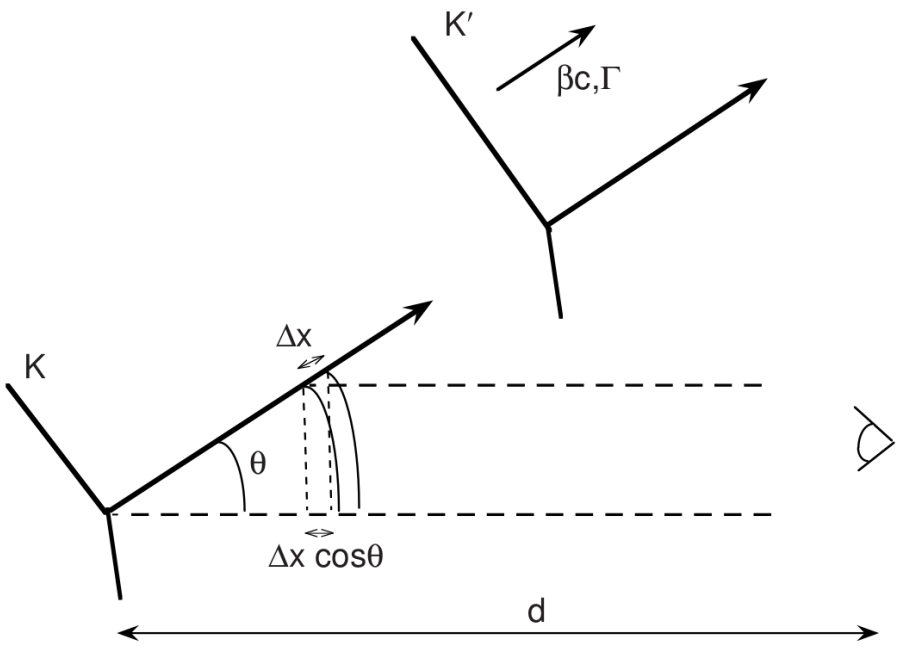

Figure 2.10: **Geometry of Doppler effect**: The photons are emitted at an angle θ with respect to the source's reference frame K' direction of motion. [8].

By subtracting equation (2.30) from (2.31) and substituting $\Delta t_* = \Delta x/\beta c$ from (2.29), we get the expression:

$$\Delta t = \frac{\Delta x}{\beta\, c}(1 - \beta\cos\theta) \tag{2.32}$$

and by taking the limit of differential quantities, we get:

$$\mathrm{d}t = \frac{\mathrm{d}x}{\beta c}(1 - \beta\cos\theta) = \Gamma \mathrm{d}t'(1 - \beta\mu) = \frac{\mathrm{d}t'}{\delta_{\mathrm{D}}}. \tag{2.33}$$

and so we get:

$$\boxed{\mathrm{d}t = \frac{\mathrm{d}t'}{\delta_{\mathrm{D}}}} \tag{2.34}$$

Finally, because $\epsilon = h\nu/m_e c^2$ and $\nu \propto 1/\Delta t$:

$$\frac{\mathrm{d}t'}{\mathrm{d}t_*} = \frac{\epsilon}{\epsilon'}. \tag{2.35}$$

2.2.3 Flux from a relativistic jet

In order to consider the flux from cosmic sources like the one arising from the emission of the relativistic jets of blazars, we have to take into account the fact that the geometry of the universe is in fact not described by the Minkowski spacetime but the Robertson-Walker metric. Without going much into detail, it is based on the exact solution of Einstein's field equations of general relativity; it describes a homogeneous, isotropic, expanding universe. In this expanding universe, there is an *absolute* reference frame, which is defined as the rest frame of the cosmic fluid, i.e, the frame that observes no dipole anisotropy in the Cosmic Microwave Background. This frame follows the 'Hubble flow', which describes the motion of galaxies due solely to the expansion of the Universe.

Since the geometry of the universe itself is expanding, it results to the phenomenon of cosmological redshift: that expansion stretches light traveling through space, causing a loss of energy and resulting in the light being redshifted. The cosmological redshift is defined as:

$$z = \frac{\lambda_{\mathrm{obs}} - \lambda_{\mathrm{em}}}{\lambda_{\mathrm{em}}} = \frac{\nu_{\mathrm{em}}}{\nu_{\mathrm{obs}}} - 1 \tag{2.36}$$

where $\lambda_{\rm em}$ refers to the wavelength of the radiation when it was emitted and $\lambda_{\rm obs}$ when it was observed. Same with the frequencies ν. Since the ratio of the frequencies is equal to the radio of the energies, and by applying the Doppler effect, we can re-write (2.36) as:

$$z = \frac{\delta_D \epsilon'}{\epsilon} - 1 \tag{2.37}$$

And therefore, we see that (2.27) and (2.34) become:

$$\epsilon = \frac{\delta_{\rm D} \epsilon'}{1+z} \tag{2.38}$$

$$dt = \frac{(1+z)dt'}{\delta_{\rm D}} \tag{2.39}$$

Radiation fundamentals and invariant quantities

To properly address the flux of cosmological sources, it is important to first introduce some fundamental quantities that are used to describe radiation.

The quantity known as intensity, denoted as I_ϵ, is defined in such a way that the product $I_\epsilon \mathrm{d}\epsilon \mathrm{d}A \mathrm{d}t \mathrm{d}\Omega$ represents the infinitesimal energy $\mathrm{d}\mathcal{E}$ carried by photons with energies between ϵ and $\epsilon + \mathrm{d}\epsilon$ that pass through a small area element $\mathrm{d}A$ oriented perpendicular to the direction $\vec{\Omega}$ during a differential time interval $\mathrm{d}t$, and within a solid angle element $\mathrm{d}\Omega$:

$$\mathrm{d}\mathcal{E} = I_\epsilon \, \mathrm{d}\epsilon \, \mathrm{d}A \, \mathrm{d}t \, \mathrm{d}\Omega \tag{2.40}$$

The differential flux for radiation coming with an angle θ to the normal is proportional to the dot product of the normal and the incidence direction:

$$\mathrm{d}F(\epsilon) = I_\epsilon \cos\theta \mathrm{d}\Omega. \tag{2.41}$$

$F(\epsilon)$ is the spectral energy flux $(\mathrm{d}\mathcal{E}/\mathrm{d}A\mathrm{d}t\mathrm{d}\epsilon)$ of radiation measured from a source that subtends a solid angle element Ω:

$$F(\epsilon) = \int d\Omega I_\epsilon \cos\theta. \tag{2.42}$$

The νF_ν energy flux ($\mathrm{d}\mathcal{E}/\mathrm{d}A\mathrm{d}t$, cgs units of ergs cm^{-2} s^{-1}) is given by:

$$f_\epsilon = \epsilon F(\epsilon) = \epsilon \int_{\Omega_s} \mathrm{d}\Omega \cos\theta I_\epsilon \tag{2.43}$$

The bolometric flux, meaning the flux in all frequencies, is derived by integrating the spectral energy flux over all energies:

$$\Phi = \int_0^\infty \mathrm{d}\epsilon F(\epsilon) = \int_0^\infty \mathrm{d}\epsilon \int_{\Omega_s} \mathrm{d}\Omega \cos\theta I_\epsilon. \tag{2.44}$$

When radiation is propagated, there could be some absorption or emission that affects the intensity of that radiation over different length paths $\mathrm{d}s$. This phenomenon is described by the radiative transfer equation:

$$\frac{\mathrm{d}I_\epsilon}{\mathrm{d}s} = -\kappa_\epsilon I_\epsilon + j(\epsilon, \Omega). \tag{2.45}$$

The first factor of the right hand side describes the absorption of the radiation, where κ_ϵ is the spectral absorption coefficient with units of inverse length. From that, we can define the optical depth $\tau_\epsilon = \kappa_\epsilon s$, which is a measure of the absorption that is taking place in a medium: the bigger the optical depth, the largest the absorption. The second factor is the emissivity, which quantifies the amount of radiation added to the radiation field per unit volume, solid angle and time:

$$\mathrm{d}\mathcal{E} = j(\epsilon, \Omega)\, \mathrm{d}V\, \mathrm{d}t\, \mathrm{d}\epsilon\, \mathrm{d}\Omega \tag{2.46}$$

Invariant quantities

Finally, the use of invariants is very helpful when calculating quantities between reference frames. The three elementary invariants are the invariant four-volume $dVdt = d^3\vec{x}dt$, the invariant phase-space element $d^3\vec{p}/E$, and the invariant phase volume $d\mathcal{V} = d^3\vec{x}d^3\vec{p}$. Hence the following quantity will also be an invariant:

$$E\frac{\mathrm{d}N}{\mathrm{d}^3\vec{x}\mathrm{d}t\mathrm{d}^3\vec{p}} = \frac{1}{\epsilon^2}\frac{\mathrm{d}\mathcal{E}}{\mathrm{d}V\mathrm{d}t\mathrm{d}\epsilon\mathrm{d}\Omega} \equiv \frac{1}{\epsilon^2}j(\epsilon,\Omega) \tag{2.47}$$

Flux from cosmological sources

Let us consider a cosmological source that is in motion relative to the Hubble flow. Quantities in its comoving frame will be denoted as primed. Additionally, there is an observer represented by unprimed quantities and a stationary emission frame that is at rest with the Hubble flow. Quantities in this frame are represented with a star symbol. The relation between the luminosity of an isotropically emitting source in the stationary emission frame $L_{*,\,\mathrm{iso}}$ and the energy flux as seen by the observer is:

$$\Phi = \frac{L_{*,\,\mathrm{iso}}}{4\pi d_L^2}. \tag{2.48}$$

Now considering a source with a directional luminosity $L_*\left(\epsilon_*,\Omega_*\right)$ and comparing with the above relation, we get:

$$F(\epsilon)d\epsilon = \frac{L_*\left(\epsilon_*,\Omega_*\right)}{d_L^2}d\epsilon_*. \tag{2.49}$$

The relations between the energies at the three frames are:

$$\epsilon = \frac{\epsilon_*}{(1+z)} = \frac{\delta_{\mathrm{D}}\epsilon'}{(1+z)}. \tag{2.50}$$

In a homogeneous and isotropic universe, the direction vector in the cosmological frame is equivalent to the direction vector in the observer frame in the sense that $\Omega_* = \Omega$. Hence we get:

$$F(\epsilon;\Omega) = \frac{(1+z)}{d_L^2}L_*\left(\epsilon_*,\Omega\right). \tag{2.51}$$

The differential luminosity is $dL_*\left(\epsilon_*,\Omega_*\right) = dV_* j_*\left(\epsilon_*,\Omega_*\right)$. We have also mentioned that the quantity $j(\epsilon,\Omega)/\epsilon^2$ is an invariant:

$$j_*\left(\epsilon_*,\Omega_*\right) = \left(\frac{\epsilon_*}{\epsilon'}\right)^2 j'\left(\epsilon',\Omega'\right). \tag{2.52}$$

Therefore, we obtain the result:

$$F(\epsilon;\Omega) = \frac{(1+z)}{\mathrm{d}_L^2}\,\delta_{\mathrm{D}}^3\,V' j'\,(\epsilon',\Omega') \tag{2.53}$$

and from that we can arrive at the expression of the energy flux by multiplying by the dimensionless energy:

$$\boxed{\epsilon F(\epsilon;\Omega) = f_\epsilon = \frac{\delta_{\mathrm{D}}^4}{d_L^2} V'\epsilon' j'\,(\epsilon',\Omega')} \tag{2.54}$$

where we used equation (2.50) for the relation between the dimensionless energies.

Flux from a spherical plasmoid-type emitter in the jet

To compute the flux coming from a jet, we approximate the emission region of the jet following the *standard one-zone blob* model, as a uniform spherical blob in the comoving frame with comoving radius R'_b and comoving volume $V'_b = 4\pi R'^3_b/3$. In addition to the single-zone model described, two-zone models are also used in which a larger, less dense emitting region is assumed. This region is typically responsible for radio emissions, while the high-energy emissions are produced by the blob (Figure 2.11).

To avoid the need of temporal interactions across various parts of the blob, it is assumed that the timescale for radiation variation, t'_{var}, is longer than the light-crossing time, which can be approximated as $t'_{\mathrm{lc}} \approx r'_b/c$, and therefore:

$$r'_b \lesssim c t'_{\mathrm{var}} = c\frac{\delta_{\mathrm{D}}\Delta t_{\mathrm{var}}}{1+z} \tag{2.55}$$

Lastly, we assume that the blob is moving with constant speed. According to equation (2.54), the flux from a relativistic blob is expressed as:

$$\epsilon F(\epsilon;\Omega) = f_\epsilon \simeq \frac{\delta_{\mathrm{D}}^4}{d_L^2} V'_b\epsilon' j'\,(\epsilon',\Omega') \tag{2.56}$$

and by assuming isotropic emission in the comoving reference frame with the blob:

$$\boxed{f_\epsilon \simeq \frac{\delta_{\rm D}^4}{4\pi d_L^2} V_b' \epsilon' j'(\epsilon') \simeq \frac{\delta_{\rm D}^4 \epsilon' L'(\epsilon')}{4\pi d_L^2}} \tag{2.57}$$

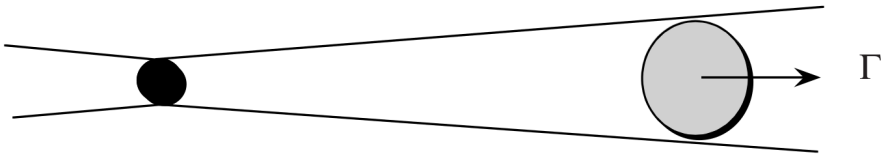

Figure 2.11: **The geometry of the emission region in the jet as approximated in the standard one-zone blob model [8].**

2.3 Modelling the high-energy emission of blazars

As we've seen, the primary source of high-energy radiation in the jets of blazars is the non-thermal emission of charged particles. Shocks (Marscher & Gear 1985 [22]) within the jet generate an overdensity that moves at relativistic speeds, which results to high-energy emission. The emission originates from radiative processes that take place within this overdensity and can be either leptonic or hadronic: leptonic radiative processes are related to electrons and positrons within the jet and hadronic radiative processes are related to protons and nuclei. The SED has a distinct two-bump structure, with the low energy bump ranging from radio to X-rays, and the high-energy bump reaching γ-ray frequencies. Even thought the first one is fairly well understood, the second bump has been the subject of intense discussion the recent years, especially after the observation of a neutrino originating from a flaring blazar which can be attributed only to hadronic processes. In this section, we will explore the different types of leptonic and hadronic emission processes, their contributions to the SED, and the ongoing debate surrounding them.

2.3.1 Leptonic emission models

In the context of leptonic models, the emission region is a blob with a powerful magnetic field and within there exist a homogeneous distribution of relativistic electrons and positrons (even though inhomogeneous models have also been proposed, e.g, Ghisellini et al. 1985 [23]). Their emission is shifted into higher frequencies, while the intensity

is increased by relativistic Doppler effect (refer to section 2.2.2). Leptonic emission models have a significant advantage in that they can account for the rapid variability observed in some blazars due to the fast cooling time of the leptons. Additionally, these models require relatively few free parameters to describe the emission region and the distribution of leptonic particles. The electron distribution is usually described by a power law, where a break sometimes is included to account for the fast radiative cooling.

Leptonic models provide a well-understood explanation for the first bump in the SED in blazars. The electrons and positrons are accelerated in the presence of the magnetic field radiating through the synchrotron process, the relativistic equivalent of the cyclotron radiation (refer to section 3.2 for a complete description of the process). However, due to synchrotron-self absorption, that is the re-absorption of the synchrotron radiation by the same electrons that radiate it, a single emitting region can not fully explain the radio frequencies, giving rise to the need of using a two-zone model for a detailed modelling of the radiation in the lower frequencies. Therefore, the radio photons are believed to originate from a different zone in much more extended regions of the jet which are further out. Nonetheless, the standard one-zone mode is sufficient to explain the high-energy emission.

In the leptonic interpretation, the second bump of the SED is explained by the process of inverse Compton radiation (refer to section 3.4.2 for a complete description of the process), in which highly relativistic electrons and positrons scatter photons into higher energies. These photons originate from the synchrotron radiation of the electrons (Konigl 1981 [24]; Inoue & Takahara 1996 [25]; Katarzyński et al. 2001 [26]) and hence the term synchrotron-self Compton (SSC). This process occurs within a single emitting region, and despite its simplicity, it can accurately fit the high-energy bump. However, in some cases, particularly for FSQRs and LBLs, the photons that are up-scattered by the electrons can also originate from an external photon field(Sikora et al. 1994 [27]), like the thermal radiation of the accretion disk, the dusty torus or the CMB. An example of a SED modelled by just leptonic emission processes is shown in Figure 2.12.

2.3.2 Motivations for hadronic modelling

Even though leptonic processes alone are able to fit the high-energy bump in the SED quite well, there are several arguments that support the existence of relativistic protons alongside the electrons in the jet. The existence of orphan flares (Krawczynski et al. 2004 [28], Böttcher 2005 [29], Sahu et al. 2013 [30]), which are an increase in brightness

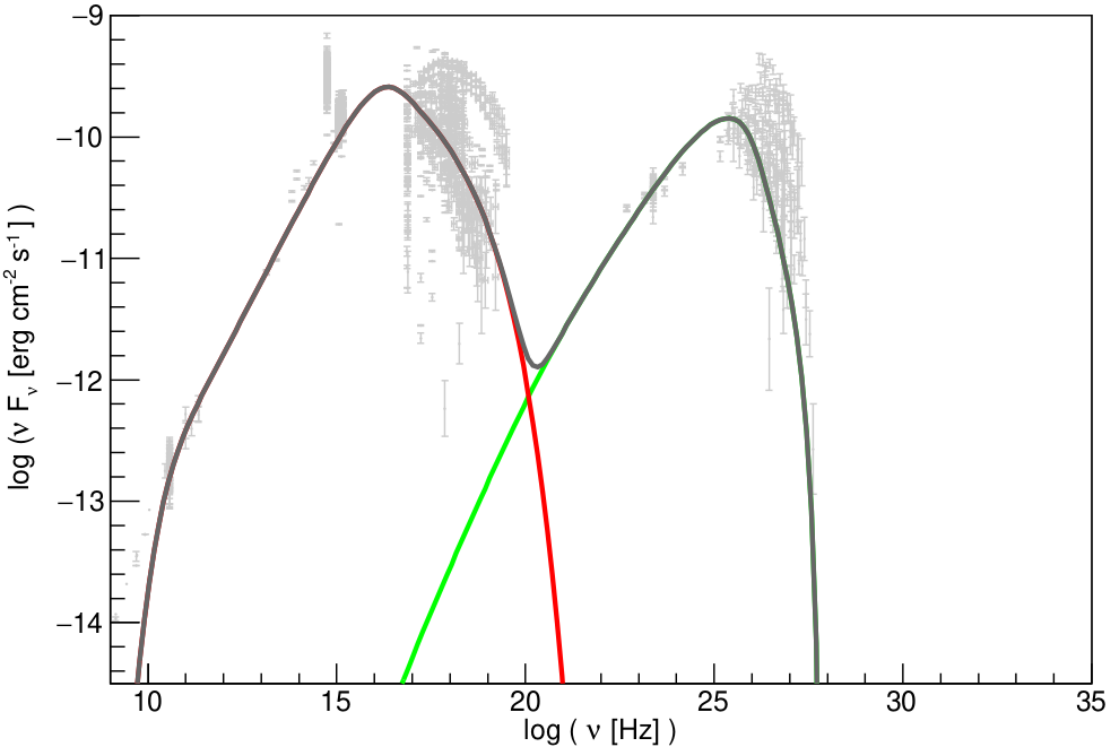

Figure 2.12: **The SED of the source Mrk421**: (Cerruti 2012 [10]) The low energy bump is modelled with electron synchrotron radiation using one emission region (one-zone modelling), while the second one is modelled with the Synchrotron Self-Compton radiation.

in just one of the two components of the spectrum (or even in just one band of the spectrum) indicates a problem for leptonic scenarios: if both the low and the high-energy components are originating from electrons, they should be correlated with each other. However, the strongest argument in favor of hadronic modelling is the multi-messenger observation of a neutrino associated with a flaring blazar in 2017. IceCube detected a muon track event on September 22, 2017 (IceCube Collaboration 2018 [31]), which was caused by a high-energy neutrino called IC-170922A. After analyzing the event's direction, it was found to coincide with the position of the γ-ray Blazar TXS 0506+056, which is situated 0.1 degrees away from the incoming direction of the high-energy neutrino. The potential neutrino productions in the jet implies that blazars can be responsible for accelerating hadrons into relativistic energies. That means that blazars can be sources of cosmic rays, the origin of which is still not fully clear. Hence, hadronic modelling is worth considering when modelling the SED of a blazar.

In leptonic models, even though the protons can be present in the emission region, they are not relativistic and therefore their emission is negligible. However, in hadronic modelling, the proton population is considered to be relativistic. In that scenario,

hadronic emission processes take place. The high-energy emission originating from the radiative processes involving protons can dominate the high-energy bump of the SED. In this case, unlike the leptonic scenario, there can be neutrino emission.

The first hadronic process to discuss is the synchrotron radiation that originates from protons (Aharonian 2000 [32]). In that case, a much stronger magnetic field or a higher particle density (or both) is required to match the luminosity of the high-energy emission we observe from blazar jets. It can become the dominant contribution and produce the high-energy bump observed in the SED (Mannheim 1993 [33]; Mücke & Protheroe 2001 [34]). The downside however is the number of free parameters: considering the free parameters that the proton distribution adds, the model becomes degenerate. That being the case, assuming some physically motivated constrains can significantly decrease this number, for instance co-acceleration of electrons and positrons. Even so, the model still remains degenerate (Cerruti et. al. 2015 [35]).

In addition to proton synchrotron radiation, photohadronic interactions may also occur, where relativistic protons interact with low-energy photons from either the electron synchrotron radiation or an external photon field. The two principal processes of photohadronic interactions are the Bethe-Heitler pair production and the photomeson process.

The photo-meson production is the interaction between an ultra-relativistic proton and a soft energy photon that results into the creation of neutral and charged mesons, mainly pions. The main interaction channels are through the Δ resonance but higher interaction channels are necessary to describe the process in detail.

$$\begin{aligned} p + \gamma &\longrightarrow p' + \pi^0 \\ p + \gamma &\longrightarrow n + \pi^+ \\ p + \gamma &\longrightarrow p' + \pi^- + \pi^+ \end{aligned} \tag{2.58}$$

The pions will then decay into neutrinos, gamma-rays, electrons and positrons:

$$\begin{aligned} \pi^0 &\longrightarrow \gamma + \gamma \\ \pi^+ &\longrightarrow \mu^+ + \nu_\mu \longrightarrow e^+ + \nu_e + \bar{\nu}_\mu + \nu_\mu \\ \pi^- &\longrightarrow \mu^- + \nu_\mu \longrightarrow e^- + \bar{\nu}_e + \bar{\nu}_\mu + \nu_\mu. \end{aligned} \tag{2.59}$$

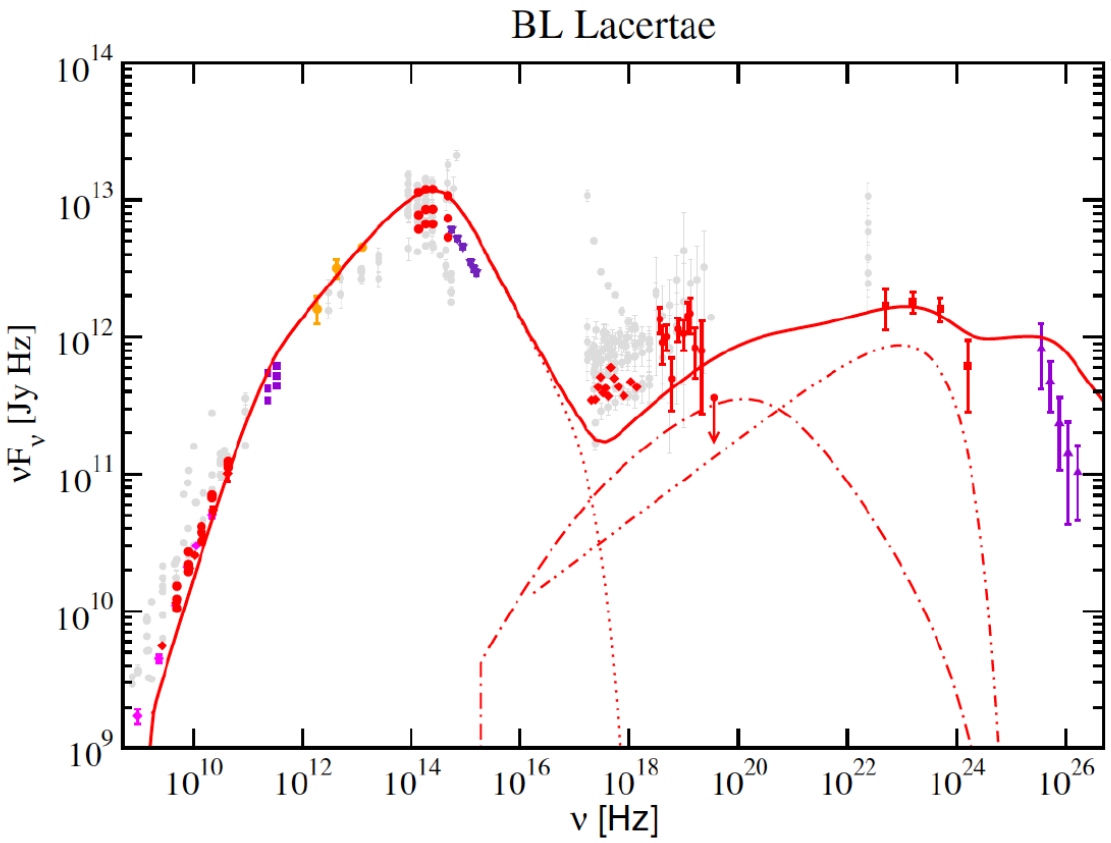

Figure 2.13: **The SED of the source IBL BL Lacertae (Böttcher et al. 2013 [11])**: The low energy bump is modelled with synchrotron radiation, while the high-energy part is attributed to contributions from the proton synchrotron, photo-meson cascade and SSC radiation.

Since neutrinos are created from such events, their detection offers compelling proof that accelerated protons are present inside the relativistic jet and thus making jetted AGNs sources of high-energy cosmic rays.

Alongside the neutrinos, high-energy photons are being created from the decay of neutral pions. They can get absorbed via pair production in the jet, initiating a synchrotron or an inverse Compton supported cascade, depending on the soft photon energy density and the magnetic fields strength. As for muons, depending on the optical depth of the emitting region, they can cool radiating synchrotron photons before decaying into electrons, positrons and neutrinos. The electrons and positrons will as well initiate an electromagnetic cascade, similarly to the photons from the neutral pion decay.

Apart from the photo-meson production, the Bethe-Heitler pair production can take place, where a photon interacts with a proton, resulting into the creation of an electron-positron pair:

$$p + \gamma \longrightarrow p + e^- + e^+. \tag{2.60}$$

The cross section of the Bethe-Heitler pair production is larger than that of the photohadronic interaction, however the energy loss of protons is significantly smaller. Therefore, photohadronic interactions will dominate the radiative output. Nonetheless, the Bethe-Heitler process is the main process of photohadronic interactions for low energy protons and should be taken into account.

Lastly, proton proton (p-p) interactions can occur: a low energy proton interacts with a high-energy one, which results similarly to the photo-meson interaction, into the production of pions that result to neutrino emission. They become relevant when the jet meets an obstacle, such as gas clouds or stars, since the jet plasma itself has a very low proton density.

2.3.3 Lepto-hadronic modelling

It is worth mentioning that hybrid scenarios such as the lepto-hadronic models are also a possibility. The magnetic field strength is the same as in the leptonic scenario and SSC is again the dominant process responsible for the high-energy bump. However, alongside electrons, there are relativistic protons as well, interacting with the low-energy photons of the electron synchrotron radiation field or an external photon field, resulting in the production of neutrinos and electron-positron pairs through photohadronic interactions. In Figure 2.13, an example of a SED modelled with both leptonic and hadronic emission processes is shown.

CHAPTER 3

The open-source package agnpy

In recent years, an increasing number of astrophysical open-source packages are being developed, based on the `NumPy` [1] package (Harris et al. 2020 [36]) for data handling, the `SciPy` [2] package (Virtanen et al. 2020[37]) for mathematical operations and the `Astropy`[3] package (Astropy Collaboration 2013, 2018 [38] [39]) for the astronomical functionality that it provides. Based on these three, they form a family of affiliated packages [4] that use the same programming formalism. This way, an international network is built among scientists that use the same software packages. That results to the constant testing and improving of these packages which are accessible to everyone.

The open-source packages developed based on the aforementioned ecosystem are few in the case of modelling the high energy emission from jetted AGNs. One option is the `Naima` package, (Zabalza 2015 [40]) used for modelling the high energy radiation from relativistic particle populations. However, even though the modelling of a relativistic jet would be possible with some adjustments, it is suited mostly for modelling the high energy radiation of unbeamed sources, making it more appropriate for galactic sources like supernova remnants. An open-source package suitable for this kind of task

[1] https://numpy.org/
[2] https://scipy.org/
[3] https://astropy.org/
[4] https://astropy.org/affiliated/#affiliated-package-list

is `JetSet` (Tramecere 2020 [41]) since it is developed specifically for sources with a relativistic jet, like micro-quasars and blazars. In the case of modelling a blazar, it allows mostly for a leptonic interpretation of the non-thermal radiation, since most of the hadronic processes are not included, apart from the proton-proton interactions (see section 2.3.2). However, the last are usually not used in blazar modelling apart from the case where the jet hits a target on its way to the Earth.

The `agnpy` [5] (Nigro et al. 2022 [42]) package is another open-source code developed for modelling the high energy emission of blazars. It includes all leptonic emission processes most commonly considered in jetted AGNs, such as synchrotron radiation, synchrotron self-absorption, inverse Compton radiation and $\gamma\gamma$ absorption. It, as well, includes the radiation from the broad line region, the dust torus and other regions that are considered to be part of an AGN. The code is time-independent, meaning that it is not developed for the time evolution of the source, however the package provides the option of constraining the model parameters in a self-consistent manner. It also provides the possibility of using data-analysis tools such as `Gammapy` (Deil et al. 2017 [43]), another open-source package used to analyze data from imaging atmospheric Cherenkov telescopes.

However, the hadronic emission processes are not included in the `agnpy` package. So far, there is no open-source package that allows for a lepto-hadronic description of the non-thermal emission of jetted AGNs.

3.1 Emission regions, target photon fields and emitters of thermal radiation

The `agnpy` package adopts the standard one-zone model (section 2 reference), where a spherical plasmoid-type emitter of radius R_b is assumed to be filled with a randomly oriented magnetic field of intensity B. All non-thermal radiative processes are considered to occur within a single emission region that corresponds to the emission region of the relativistic jet. Electrons (and positrons) that emit radiation are confined within this region and are assumed to have a homogeneous and isotropic distribution in the emission region's reference frame. All non-thermal emission processes are modelled following Dermer & Menon 2009 [8] and Finke et al. 2008 [44].

The package provides different photon fields as targets to the inverse Compton and $\gamma\gamma$

[5] https://github.com/cosimoNigro/agnpy

processes. They originate from either thermal or line emitters. The emitters available in the package are: the cosmic microwave background, the Shakura & Sunyaev accretion disk (Shakura & Sunyaev 1973 [45]) modelled as a thin disk whose emission is parameterized following Dermer & Schlickeiser 2002 ([46]) and Dermer et al. 2009 ([47]), the broad line region approximated as a thin sphere that reprocesses a fraction of the disks radiation in a monochromatic emission (Finke 2016 [48]), a dust torus simplified to a ring reprocessing a fraction of the disks radiation in a single-temperature black body emission and a monochromatic point-like source behind the emission region, mostly for consistency tests. The thermal radiation for some of these emitters is available: It is possible to model the multi-temperature black body emission that originates from the accretion disk or the dust torus.

3.2 Synchrotron radiation

For the description of the synchrotron radiation and for the rest of the non-thermal radiative processes described in this and the next sections, Dermer & Menon 2009 [8] and Finke et al. 2008 [44] are closely followed.

The emission of radiation known as synchrotron radiation occurs when a relativistic charged particle undergoes acceleration in the presence of a magnetic field. The Lorentz force in this context can be expressed as:

$$\vec{F}_L = \frac{\mathrm{d}}{\mathrm{d}t}(\gamma m \vec{v}) = Q\left(\vec{E} + \frac{1}{c}\,\vec{v} \times \vec{B}\right) \tag{3.1}$$

Here, $\vec{E}$ represents the electric field vector, $\vec{B}$ the magnetic field vector, $\vec{v}$ the particle velocity vector, and Q the particle's charge. In astrophysical plasma environments, the conductivity is high, and therefore, the total electric field can be approximated to be zero. As a result, the expression for the Lorentz force in Equation (3.1) reduces to:

$$\frac{\mathrm{d}\vec{v}}{\mathrm{dt}} = Q\,\frac{\vec{v} \times \vec{B}}{\gamma m c} \equiv \omega_L \left(\vec{v} \times \frac{\vec{B}}{B}\right) \tag{3.2}$$

where ω_L is the Larmor angular frequency and is given by:

$$\omega_L = 2\pi\nu = \frac{QB}{\gamma mc} = \frac{\Omega}{\gamma} \tag{3.3}$$

.

The Larmor angular frequency characterizes the precession rate of the magnetic moment of the particle around an external magnetic field and Ω its the non-relativistic gyro-frequency. The Larmor radius is defined as the radius of that gyration:

$$\omega_L \, r_L = v_\perp = \beta_\perp c = \beta \, c \sin\psi \tag{3.4}$$

where $\vec{\beta} = \vec{v}/c$ is the beta factor and ψ denotes the pitch angle of the particle, i.e., the angle between the particle's velocity and the direction of the magnetic field vector (refer to Figure 3.1). By solving equation (3.4) for the Larmor radius, we get:

$$r_L = \frac{\beta\gamma mc^2 \sin\psi}{QB}. \tag{3.5}$$

In the case of a pitch angle of $\pi/2$, the above relation simplifies to:

$$r_L = \frac{E}{QB} \tag{3.6}$$

where $E = \gamma mc^2$ is the energy of the particle.

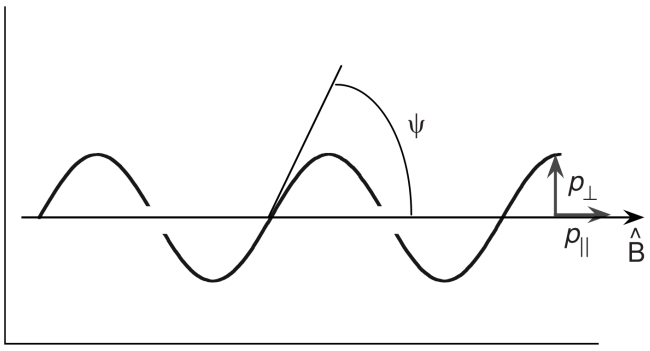

Figure 3.1: **Spiraling of a charged particle in a magnetic field:** A charged particle spiraling in a uniform magnetic field $\vec{B}$ with momentum p and a pitch angle ψ. [8]

3.2.1 Calculation of the synchrotron power

The Larmor formula is essential in computing the synchrotron power, which refers to the radiated power in a particular direction $\hat{n}$ (the derivation can be found in (Rybicki, G. B., and Lightman, A. P. 1991 [9]). It is expressed as:

$$\frac{\mathrm{d}P}{\mathrm{d}\Omega} = \frac{Q^2}{4\pi c} \frac{\mid \hat{n} \times [(\hat{n} - \vec{\beta}) \times \dot{\vec{\beta}}] \mid}{(1 - \hat{n} \cdot \vec{\beta})^5}. \tag{3.7}$$

It is simpler to calculate the synchrotron power in a reference frame where the pitch angle ψ is equal to 90^o. In order to obtain the synchrotron power for different pitch angles, a Lorentz boost should be applied. In the $\psi = 90^o$ frame, the charged particle's velocity is given by:

$$\vec{\beta} = \beta(\hat{x} \cos \omega_L t + \hat{y} \sin \omega_L t). \tag{3.8}$$

The total spectral energy emitted per revolution at radial frequency $\omega = 2\pi\nu$ is obtained by solving the equation (3.7). Averaged over both polarization modes, it is given by:

$$I^{\mathrm{syn}}(\omega) = \frac{\mathrm{d}E}{\mathrm{d}\omega} = \frac{2e^2\omega}{\sqrt{3}\gamma^2\omega_L c} \int_{2\omega/3\omega_L\gamma^2}^{\infty} \mathrm{d}\xi \, K_{5/3}(\xi). \tag{3.9}$$

Therefore, the emitted spectral energy at frequency $\nu = \omega/2\pi$ is:

$$I^{\mathrm{syn}}(\nu) = \frac{\mathrm{d}E}{\mathrm{d}\nu} = \frac{1}{2\pi}\frac{\mathrm{d}E}{\mathrm{d}\omega} = \frac{1}{2\pi} I^{\mathrm{syn}}(\omega) \tag{3.10}$$

The radiated power, then, at frequency $\nu = \omega_L/2\pi$ since the particle's radial velocity is ω_L, is:

$$P^{\mathrm{syn}}(\nu) = \frac{\mathrm{d}E}{\mathrm{d}t\,\mathrm{d}\nu} = \omega_L I^{\mathrm{syn}}(\nu) \tag{3.11}$$

In the case of electrons, the critical frequency is given by:

$$\nu_c = \frac{3}{2}\left(\frac{eB}{2\pi m_e c}\right). \tag{3.12}$$

By combining the equations (3.9), (3.11) and (3.12), we derive the total instantaneous power emitted by an electron with pitch angle $\psi = \pi/2$ around a uniform magnetic field with strength B as:

$$P^{\rm syn}(\nu) = \frac{\sqrt{3}e^3\,B}{m_e c^2}\left(\frac{\nu}{\nu_c}\right)\int_{\nu/\nu_c}^{\infty} {\rm d}\xi\; K_{5/3}(\xi). \tag{3.13}$$

By using the dimensionless energy notation $\epsilon = h\nu/m_e c^2$, we define:

$$F(x) \equiv x\int_x^{\infty} {\rm d}\xi K_{5/3}(\xi) \rightarrow \begin{cases} \dfrac{4^3 B}{\Gamma(1/3)h}\left(\dfrac{\epsilon}{\epsilon_c}\right)^{1/3} & ,\epsilon \ll \epsilon_c \\ \\ \sqrt{\dfrac{3\pi}{2}}\dfrac{e^3 B}{h}\sqrt{\dfrac{\epsilon}{\epsilon_c}} & ,\epsilon \gg \epsilon_c. \end{cases} \tag{3.14}$$

We can, then, write (3.13) as:

$$P^{\rm syn}(\epsilon) = \left.\frac{dE}{dtd\epsilon}\right|_{\rm syn} = \frac{\sqrt{3}e^3 B}{h}\left(\frac{\epsilon}{\epsilon_c}\right)\int_{\epsilon/\epsilon_c}^{\infty} d\xi\; K_{5/3}(\xi) = \frac{\sqrt{3}e^3 B}{h}F_{\rm syn}(x). \tag{3.15}$$

which we are going to use later in this section.

3.2.2 Relevant reference frames and transformations

Since we know the power in the 90^o pitch-angle reference frame, we have to perform the proper transformation in order to derive the power in the emission frame. In Figure 3.2, the relations between the emission frame K_*, the 90^0 pitch-angle frame K' and the reception reference frame K are shown. Primed quantities will refer to quantities in the 90^0 pitch-angle frame K', while the unprimed ones to the emission frame K_*. All the relativistic transformations that we use in this section are explained in detail in section 2.2.2.

The instantaneous power between the emission frame K_* and the 90^o pitch-angle frame K' is invariant, since the electrons radiate with forward-backward symmetry. Specifically, if $\gamma_{\parallel}$ is the Lorentz factor between K' and K_*, then the relation between the frequency in the two frames is:

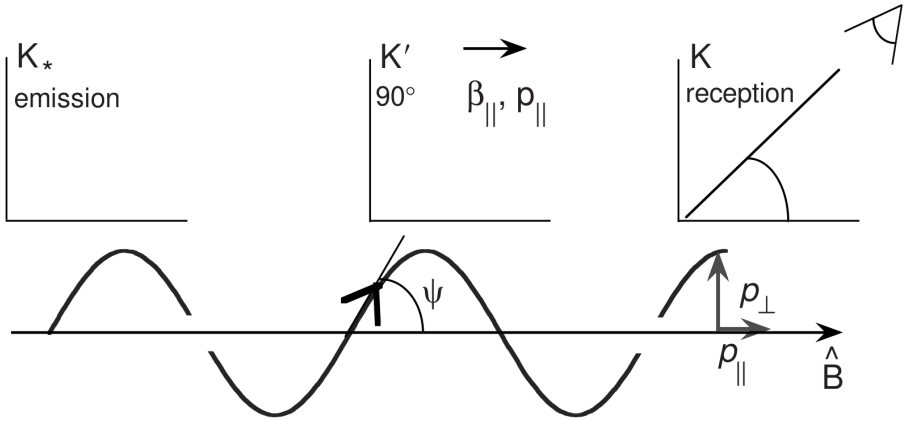

Figure 3.2: **Illustration of the stationary emission frame, the 90^o pitch-angle frame and the reception frame in the calculation of the Synchrotron radiation coming from a relativistic blob**: The Lorentz factor γ of the radiating electron in the emission frame K_* is $\gamma = \gamma'/\sin\psi$, where γ' is the Lorentz factor of the electron in the 90^o pitch-angle frame. [8]

$$\nu = \gamma_{\|}\,\nu'(1+\beta\cos\theta') \Rightarrow \langle\nu\rangle = \gamma_{\|}\nu' \tag{3.16}$$

considering the mean photon emission frequency $\langle\nu\rangle$, averaged over θ'. The time dilation is:

$$\mathrm{d}t = \gamma_{\|}\,\mathrm{d}t'. \tag{3.17}$$

Hence:

$$P'^{\,\mathrm{syn}} = \frac{\mathrm{d}E'}{\mathrm{d}t'} = h\nu'\frac{\mathrm{d}N}{\mathrm{d}t'} = h\langle\nu\rangle\frac{\mathrm{d}N}{\mathrm{d}t'} = \frac{\mathrm{d}E}{\mathrm{d}t} = P^{\,\mathrm{syn}} \tag{3.18}$$

since the $\gamma_{\|}$ vanish. The specific powers are related by $P'^{\,\mathrm{syn}}(\nu')\mathrm{d}\nu' = P^{\,\mathrm{syn}}(\nu)\mathrm{d}\nu$, therefore:

$$P^{\,\mathrm{syn}}(\nu) = P^{\,\mathrm{syn}}(\nu;\psi) = \left|\frac{\mathrm{d}\nu'}{\mathrm{d}\nu}\right| P'^{\,\mathrm{syn}}(\nu') \cong \sin\psi\; P'^{\,\mathrm{syn}}(\nu'). \tag{3.19}$$

Because of the relativistic beaming:

$$\gamma_{\parallel} = \frac{1}{\sqrt{1-\beta_{\parallel}^2}} = \frac{1}{1-\beta^2\cos\psi^2} \cong \frac{1}{\sin\psi}, \tag{3.20}$$

therefore:

$$\nu' = \langle\nu\rangle/\gamma_{\parallel} = \sin\psi\ \nu. \tag{3.21}$$

Thereupon, from equations (3.13), (3.19) and (3.21), the emitted synchrotron spectral power for an electron with pitch angle ψ spiraling in an ordered magnetic field is given by:

$$P^{\rm syn}(\nu) = \frac{\sqrt{3}e^3\,B}{mc^2}\left(\frac{\nu}{\bar{\nu}_c}\right)\ \sin\psi\int_{\nu/\bar{\nu}_c}^{\infty}{\rm d}\xi\ K_{5/3}(\xi) \tag{3.22}$$

where $\bar{\nu}_c = \nu_c\,\sin\psi$.

However, we are interested in the flux observed in the receivers frame K. From this point on-wards, unprimed quantities will refer to the K frame, while primed will still refer to the 90^o pitch-angle frame K'. The specific spectral energy is given by:

$$P(\nu,\Omega) = \frac{{\rm d}E}{{\rm d}t{\rm d}\nu{\rm d}\Omega} = h\nu^2\left(\frac{{\rm d}N}{\nu{\rm d}\nu{\rm d}t{\rm d}\Omega}\right). \tag{3.23}$$

The invariance of $E{\rm d}N/d^3\vec{p}$ for photons implies that $E^{-1}({\rm d}N/{\rm d}E{\rm d}\Omega)$ is also invariant, since $d^3\vec{p} = p^2{\rm d}p\Omega$ and $E = cp$. Therefore, since $E^{-1}({\rm d}N/{\rm d}E{\rm d}\Omega) = {\rm d}N/\nu{\rm d}\nu{\rm d}\Omega$ because of $E = h\nu$, then the term ${\rm d}N/\nu{\rm d}\nu{\rm d}\Omega$ is also invariant. Also, $\nu = \delta_{\rm D}\nu'$ and ${\rm d}t = {\rm d}t'/\delta_{\rm D}$. Thus, the relation between the specific spectral powers is given by:

$$P^{\rm syn}_{\rm rec}(\nu,\Omega) = \delta_{\rm D}^3 P'^{\rm syn}\left(\nu',\Omega'\right). \tag{3.24}$$

By averaging over angles, two powers of δ_D are removed, resulting to the expression:

$$P^{\rm syn}_{\rm rec}(\nu) = \delta_{\rm D} P'^{\rm syn}\left(\nu'\right). \tag{3.25}$$

For relativistic electrons:

$$\mu' = \frac{\pi}{2} + \mathcal{O}\left(\frac{1}{\gamma'}\right) \tag{3.26}$$

and therefore, we can approximate the Doppler factor as:

$$\delta_{\rm D} = \left[\gamma_{\parallel}\left(1 - \beta_{\parallel}\mu\right)\right]^{-1} = \gamma_{\parallel}\left(1 + \beta_{\parallel}\mu'\right) \cong \gamma_{\parallel} \cong \frac{1}{\sin\psi} \tag{3.27}$$

Where in the last step, we used equation (3.20). Therefore, the relation between the receivers frame K and the 90^o pitch-angle frame K' can be written as:

$$P^{\rm syn}_{\rm rec}(\nu) = \delta_{\rm D} P'^{\rm syn}\left(\nu'\right) = \frac{P'^{\rm syn}\left(\nu'\right)}{\sin\psi}. \tag{3.28}$$

By using equation (3.19), we can finally write the relation between the emission frame K_* and the receivers frame K:

$$P^{\rm syn}_{\rm rec}(\nu) = \frac{P^{\rm syn}_{\rm em}(\nu)}{\sin^2\psi}. \tag{3.29}$$

We see that changes in the average distance between an electron and an observer account for the difference between received and emitted power. Therefore, as long as the average distance between a distribution of electrons and an observer remains constant, the received and emitted powers will be equal (Blumenthal & Gould 1970 [49], Rybicki, G. B., and Lightman, A. P. 1991 [9]).

From these considerations and by using equation (3.15), we can express the total spectral luminosity of a synchrotron emitting region in the emission frame as:

$$L^{\rm syn}_{\nu} = \frac{{\rm d}E}{{\rm d}\nu{\rm d}t} = \frac{\sqrt{3}e^3 B}{m_e c^2} \oint d\Omega_{\psi} \sin\psi \int_1^{\infty} {\rm d}\gamma \; N_e(\gamma, \Omega_{\psi}) F(x) \tag{3.30}$$

where $x = \nu/\bar{\nu}_c$. Here, $N_e(\gamma) = V\, n_e(\gamma)$ is the electron distribution that emit the synchrotron radiation, with a general pitch-angle distribution in a randomly ordered magnetic field, multiplied by the volume of the emitting region. From this, an analytic expression for the pitch-angle-averaged synchrotron spectral power can be derived (Crusius, A. and Schlickeiser, R. 1986 [50]):

$$\langle P^{\rm syn}(\nu)\rangle = \frac{\sqrt{3}e^3 B}{m_e c^2}\int_1^\infty {\rm d}\gamma\, N_e(\gamma)\, R(x) \tag{3.31}$$

where $x = \nu/\nu_c$, and:

$$R(x) = \frac{x}{2}\int_0^\pi {\rm d}\theta\, \sin\theta \int_{x/\sin\theta}^\infty {\rm d}t\, K_{5/3}(t). \tag{3.32}$$

which represents the pitch-angle-averaged synchrotron spectral power of a single electron. A good approximation to $R(x)$ is provided by F.A. Aharonian, S.R. Kelner, and A.Y. Prosekin 2010 [51] with better than 0.2% accuracy:

$$R(x) \simeq \frac{1.808\, x^{1/3}}{\sqrt{1+3.4\, x^{2/3}}}\frac{1+2.21\, x^{2/3}+0.347\, x^{4/3}}{1+1.353\, x^{2/3}+0.217\, x^{4/3}}e^{-x}. \tag{3.33}$$

The observed synchrotron flux in the receivers frame, originating from a relativistic blob, following equation (2.57), is then given by the expression:

$$\boxed{\nu F_\nu^{\rm syn} = f_\epsilon^{syn} = \frac{\delta_D^4\, \nu' \langle P'^{\,\rm syn}(\nu')\rangle}{4\pi d_L^2}} \tag{3.34}$$

where now the prime quantities refer to the emission frame and not the 90^o pitch-angle frame, therefore $\nu' = \delta_D\, \nu/(1+z)$.

3.3 Synchrotron self-absorption

When the intensity of the synchrotron radiation within the source is sufficiently high, then the electrons themselves can re-absorb the radiation. In the case of a relativistic blob, the synchrotron flux density (R. J. Gould 1979 [52]) is given by:

$$S_\nu = \frac{j(\nu)}{2\kappa}\left(\frac{r_b}{d_L}\right)^2 u(\tau) = \frac{j(\nu)\, V_b}{4\pi\, d_L^2}\frac{3u(\tau)}{\tau}. \tag{3.35}$$

Here j_ν is the non-thermal synchrotron emissivity and τ is the frequency depended optical depth,defined as:

$$\tau_{SSA} \equiv 2\kappa_\nu r_b \tag{3.36}$$

where κ_ν is the frequency depended synchrotron self-absorption (SSA) coefficient and $u(\tau)$ is given by:

$$u(\tau) = \frac{1}{2}\frac{\exp(-\tau)}{\tau} - \frac{1-\exp(-\tau)}{\tau^2} = \frac{1}{2}\left(1 - \frac{2}{\tau^2}\left[1-(1-\tau)\exp(-\tau)\right]\right). \tag{3.37}$$

The synchrotron self-absorbed flux as observed in the receivers frame is then given by:

$$\boxed{\nu F_\nu^{\rm syn} = f_\epsilon^{syn} = \frac{3u(\tau)}{\tau}\,\frac{\delta_D^4\,\nu'\langle P'^{\,\rm syn}(\nu')\rangle}{4\pi d_L^2}} \tag{3.38}$$

where prime quantities refer to the emission frame, therefore $\nu' = \delta_D\,\nu/(1+z)$.

3.3.1 Einstein coefficients

In order to derive the SSA coefficient, we first have to review the Einstein's coefficients. We consider an atom with with electron energy states W_1 and W_2, where $W_2 > W_1$. When such an atom interacts with radiation, there are three main processes that can occur:

1. spontaneous emission, where initially the atom is in the higher energy state and it decays to the lower one, emitting a photon of energy $W2 - W1$. The Einstein coefficient in this case is the transition probability per unit time and it is represented by A_{21}.

2. Absorption, where the atom initially is in the lower energy states and it absorbs a photon of energy $W_2 - W_1$, going to the higher level. The absorption is not monochromatic and therefore it is described by the distribution $\phi(\nu)$, peak at the frequency ν_0 corresponding to the energy $W_2 - W_1$. If J_ν is the mean intensity of the external radiation field, then the absorption probability per unit time is equal to:

$$B_{12}\int_0^\infty J_\nu\,\phi(\nu)\mathrm{d}\nu. \tag{3.39}$$

3. Stimulated emission, which is a consequence of light's quantum nature. The atom initially is in the higher energy state and it decays in the lower one in the presence of a radiation field. The transition probability per unit time is:

$$B_{21} \int_0^\infty J_\nu \, \phi(\nu) \mathrm{d}\nu. \tag{3.40}$$

At this point, we consider a two-level atom population with electron energy states N_1 and N_2 with occupancy numbers g_1 and g_2 respectively. In thermal equilibrium, they follow the Boltzmann distribution:

$$\frac{N_1}{N_2} = \frac{g_1}{g_2} \exp\left(\frac{h\nu_{21}}{k_B T}\right) \tag{3.41}$$

where $h\nu_{21} = W_2 - W_1$. In steady state, the sum of the spontaneous and stimulated rates from the higher to the lower state must be equal to the absorption rate from the lower to the higher state. Hence:

$$N_2[A_{21} + I_\nu(\Omega) B_{21}] = N_1 B_{12} \, I_\nu(\Omega) \tag{3.42}$$

3.3.2 Calculation of the Synchrotron Self-Absorption coefficient

The absorption coefficient results from both the "true" absorption which is proportional to $N_1 I_\nu(\Omega) B_{21}$ and the stimulated emission which is proportional to $N_2 I_\nu(\Omega) B_{21}$. Thus, the SSA coefficient is:

$$\kappa_\nu = \frac{h\nu}{4\pi} \sum_{W_1} \sum_{W_2} [\, n(W_1) B_{12} - n(W_2) B_{21} \,] \phi_{12}(\nu) \tag{3.43}$$

where ϕ_{21} is the line profile function (units in Hz^{-1}) and ensures that $h\nu = W_2 - W_1$. By expressing the energy $n(W_1)$ as $n(W_2 - h\nu)$ and by substituting equation (3.41), we get:

$$\kappa_\nu = \frac{h\nu}{4\pi} \sum_{W_2} \left[\left(\frac{g_2}{g_1} n(W_2 - h\nu) - n(W_2) \right) \sum_{W_1} B_{21} \phi_{12}(\nu) \right] \tag{3.44}$$

The average power per unit frequency from levels W_2 to level W_1 is equal to:

$$P(\nu, W_2) = h\nu \sum_{W_1} A_{21}\phi_{21}(\nu) = \frac{2h^2\nu^4}{c^2} \sum B_{21}\,\phi_{21}(\nu) \tag{3.45}$$

therefore, by substituting equation (3.45) into (3.44) we get:

$$\kappa_\nu = \frac{c^2}{8\pi h\nu^3} \sum_{W_2} P(\nu, W_2) \left(\frac{g_2}{g_1} n(W_2 - h\nu) - n(W_2) \right) \tag{3.46}$$

For the elementary quantum states, $g_1 = g_2$, and:

$$\sum_i n(W_i) \longrightarrow \int \mathrm{d}^3\vec{p}\, f(\vec{p}) \tag{3.47}$$

$$W_2 - h\nu \longrightarrow p_2^*. \tag{3.48}$$

and by using a particle distribution function formulation where $f(\vec{p}) = \mathrm{d}N/\mathrm{d}V\,\mathrm{d}^3\vec{p}$, (3.46) becomes:

$$\kappa_\nu = \frac{c^2}{8\pi h\nu^3} \int \mathrm{d}^3\vec{p_2} \left[f(\vec{p_2^*}) - f(\vec{p_2}) \right] P(\nu, W_2) \tag{3.49}$$

Finally, for processes that are continuously lousing energy, $f(W_2 - h\nu) - f(W_2) = -h\nu\,\partial f/\partial p$. Therefore, the SSA coefficient is given by:

$$\boxed{\kappa_\nu = -\frac{c^2}{8\pi m_e \nu^2} \int \mathrm{d}\gamma\; P(\nu, \gamma) \left[\gamma^2 \frac{\partial}{\partial \gamma} \left(\frac{n(\gamma)}{\gamma^2} \right) \right]} \tag{3.50}$$

3.4 Compton scattering

Compton scattering is the phenomenon where an electron is getting scattered by a photon with a comparable energy. In that case, the photon will transfer a part of its energy to the electron. However, when the electron is moving at relativistic speeds, it is possible for inverse Compton scattering to occur, in which this time the photon is the

one that gains energy. In order to describe in detail the phenomenon, it is necessary to examine the behaviour of the Compton cross section.

3.4.1 Compton effect

Consider a photon with scattering an electron in the electron rest frame (ERF). In that case, the electron has initially a Lorentz factor equal to 1 and the photon a dimensionless energy $\epsilon = h\nu/mc^2$. After the scattering, the electron gains energy and has a Lorentz factor $\gamma_e = 1/\sqrt{1-\beta_e^2}$, getting scattered in the direction θ_e with respect to the incident photon direction, like shown in Figure 3.3. The energy conservation reads as:

$$1 + \epsilon = \epsilon_s + \gamma_e \tag{3.51}$$

where ϵ_s is the photon's energy after the scattering, while the conservation of momenta in the directions parallel and transverse to the initial photon direction is:

$$\epsilon = \epsilon_s \cos\chi + \beta_e\gamma_e \cos\theta_e \tag{3.52}$$

$$\epsilon_s \sin\chi = \beta_e\gamma_e \sin\theta_e, \tag{3.53}$$

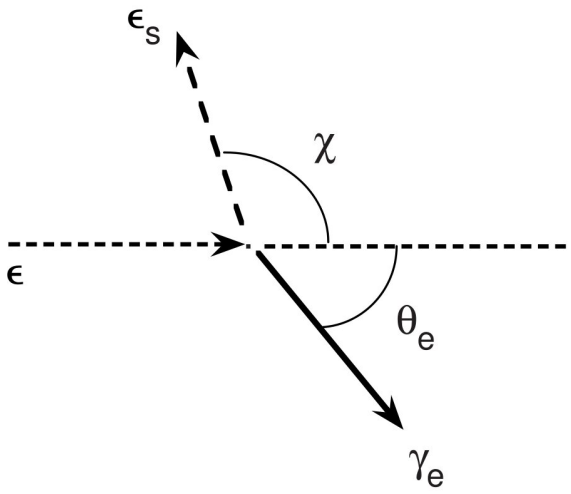

Figure 3.3: **Compton scattering:** In the electrons rest frame, an electron is getting scattered by a photon, gaining energy. After the scattering, the electron has a Lorentz factor equal to γ_e, while the photon energy equal to ϵ_s[8].

By solving the system, we arrive at the following relation for the photon's energy after the scattering:

$$\epsilon_s = \frac{\epsilon}{1 + \epsilon(1 - \cos\chi)}. \tag{3.54}$$

If the incident photon energy in the ERF is $\epsilon \ll 1$, then the scattering is approximately elastic, meaning that the photon does not louse energy. This is the Thomson regime. Otherwise, the Klein-Nishina regime arises when $\epsilon \gg 1$.

The polarized-averaged Klein-Nishina differential Compton cross section in the ERF is reported to be:

$$\frac{\mathrm{d}\sigma_\mathrm{C}}{\mathrm{d}\epsilon_s \mathrm{d}\Omega_s} = \frac{r_e^2}{2}\left(\frac{\epsilon_s}{\epsilon}\right)^2 \left(\frac{\epsilon_s}{\epsilon} + \frac{\epsilon}{\epsilon_s} - 1 + \cos^2\chi\right) \delta\left(\epsilon_s - \frac{\epsilon}{1 + \epsilon(1 - \cos\chi)}\right) \tag{3.55}$$

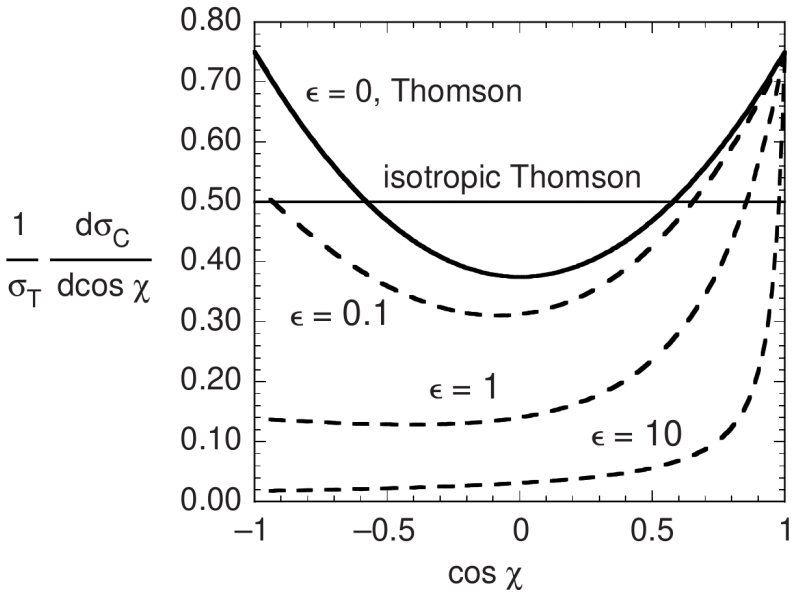

Figure 3.4: **The differential cross section of Compton scattering**: The differential cross section $d\sigma_\mathrm{C}/d\cos\chi$ as a function of the cosine of the scattering angle, $\cos\chi$ is plotted for different values of incident photon energy ϵ. The limiting Thomson form of the differential cross section is shown by the heavy solid curve, and the isotropic cross section in the Thomson limit is shown by the light solid line. [8]

where,

$$\mathrm{d}\Omega_s = \mathrm{d}\phi_s \mathrm{d}\cos\chi. \tag{3.56}$$

Here, $r_e = e^2/m_e c^2$ is the the classical electron radius and $\sigma_{\rm T} = 8\pi r_e^2/3$ the Thomson cross section.

We obtain the angle-depended Klein-Nishina cross section after integrating the equation (3.55) over the scattered photon energy:

$$\frac{\mathrm{d}\sigma_{\rm C}}{\mathrm{d}\Omega_s} = \frac{r_e^2}{2}\left[1+\epsilon(1-\cos\chi)^2\right]\left(\frac{1}{1+\epsilon(1-\cos\chi)} + \cos^2\chi + \epsilon(1-\cos\chi)\right) \tag{3.57}$$

while in the Thomson regime, the differential cross section becomes:

$$\frac{\mathrm{d}\sigma_{\rm T}}{\mathrm{d}\Omega_s} = \frac{r_e^2}{2}\left(1+\cos\chi^2\right). \tag{3.58}$$

3.4.2 Inverse Compton scattering

In order to describe the process of inverse Compton scattering, we will proceed as follows. We already know how to treat Compton scattering in the ERF. We therefore can Lorentz boost to the ERF and apply our results of regular Compton scattering and then boost back to the scattering frame (SF). The scattering frame in the context of blazars, is the comoving frame of relativistic plasma ejected by the black hole. In our description, that is the blob (the emission frame of 3.2.2). The unprimed quantities are now referring to the SF, while quantities on the ERF are denoted by overbars. The frames are shown in Figure (3.5). By remembering equation (3.54), we can write the energy of the scattered photon in the ERF as:

$$\bar{\epsilon}_s = \frac{\bar{\epsilon}}{1+\bar{\epsilon}(1-\cos\bar{\chi})} \approx \bar{\epsilon} \tag{3.59}$$

where we approximate the Compton scattering in the ERF to be in the Thompson regime. The Lorentz transformation from the SF to the ERF, of the incident photon energy is given by (refer to section 2.2.2) :

$$\bar{\epsilon} = \gamma\epsilon\left(1-\beta_e\cos\psi\right) \tag{3.60}$$

where ψ is the angle between the incident photon direction and the scattered electron

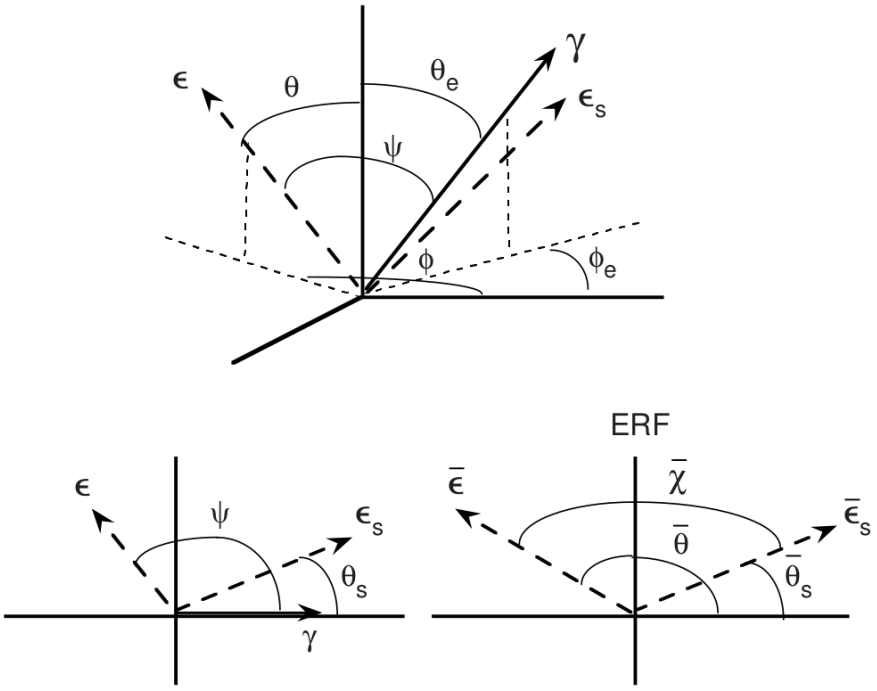

Figure 3.5: **Inverse Compton scattering**: An electron with Lorentz factor γ scatters a photon with energy ϵ to the energy ϵ_s. The Compton scattering in the electron rest frame (ERF) is demonstrated on the lower right panel while in the scattering frame, on the lower left and upper panels. Quantities in the ERF are denoted by overbars. [8]

in the SF. However, $\bar{\epsilon}_s = \bar{\epsilon}$ since in the ERF the scattering is in the Thompson regime, therefore:

$$\bar{\epsilon}_s = \bar{\epsilon} = \gamma\epsilon\left(1 - \beta_e \cos\psi\right). \tag{3.61}$$

The transform back from the ERF to the SF is:

$$\epsilon_s = \gamma\bar{\epsilon}_s\left(1 + \beta_e \cos\bar{\theta}_s\right) \tag{3.62}$$

and by substituting equation (3.61) to the above expression, we obtain the energy of the scattered photon in the SF frame:

$$\epsilon_s = \gamma^2\epsilon\left(1 - \beta_e \cos\psi\right)\left(1 + \beta_e \cos\bar{\theta}_s\right). \tag{3.63}$$

which in the limit of $\gamma \gg 1, \beta_e \to 1$, the scattered photons have energies as large as

$\epsilon_s \cong 4\gamma^2\epsilon$. We see that for relativistic electrons, the photons will generally gain energy. For the photons to actually transfer energy to the electron, it should be $4\gamma\epsilon \ll 1$ which is the Thomson condition.

3.4.3 The head-on approximation

In the limit of $\gamma \gg 1, \beta_e \to 1$, when viewed in the ERF the photon is travelling approximately at the same direction as the electron, except for a few photons that are inside a code of solid angle element of about $1/\gamma^2$ due to relativistic beaming. That is expressed by:

$$\cos\bar{\theta} = \frac{(\cos\psi - \beta_e)}{(1 - \beta_e \cos\psi)} \to -1 \tag{3.64}$$

in the $\gamma \gg 1$ limit. In that case, since the photons are scattered back approximately in the same direction as the incident electrons, $\cos\bar{\chi} \approx -\cos\bar{\theta}_s$. The differential cross section in the ERF given by the equation (3.55) gets simplified and becomes:

$$\frac{\mathrm{d}\sigma_{\mathrm{C}}(\bar{\epsilon})}{\mathrm{d}\bar{\epsilon}_s \mathrm{d}\bar{\Omega}_s} \longrightarrow \frac{r_e^2}{2}\left(\frac{\bar{\epsilon}_s}{\bar{\epsilon}}\right)^2 \left(\frac{\bar{\epsilon}_s}{\bar{\epsilon}} + \frac{\bar{\epsilon}}{\bar{\epsilon}_s} - 1 + \bar{\mu}_s^2\right) \times \delta\left(\bar{\epsilon}_s - \frac{\bar{\epsilon}}{1 + \bar{\epsilon}\,(1 + \bar{\mu}_s)}\right). \tag{3.65}$$

Due to the invariance of $\mathrm{d}\sigma/\epsilon\,\mathrm{d}\epsilon\,\mathrm{d}\Omega$ for photons:

$$\frac{\mathrm{d}\sigma_{\mathrm{C}}}{\mathrm{d}\epsilon_s \mathrm{d}\Omega_s} = \frac{\epsilon_s}{\bar{\epsilon}_s}\frac{\mathrm{d}\sigma_{\mathrm{C}}}{\mathrm{d}\bar{\epsilon}_s \mathrm{d}\bar{\Omega}_s} \tag{3.66}$$

and therefore we can approximate the differential Compton-scattering cross section in the SF, by the expression:

$$\frac{\mathrm{d}\sigma_{\mathrm{C}}}{\mathrm{d}\epsilon_s \mathrm{d}\Omega_s} \cong \delta\left(\Omega_s - \Omega_e\right)\frac{\mathrm{d}\sigma_{\mathrm{C}}}{\mathrm{d}\epsilon_s} \cong \delta\left(\Omega_s - \Omega_e\right)\oint \mathrm{d}\bar{\Omega}_s \left(\frac{\epsilon_s}{\bar{\epsilon}_s}\right)\frac{\mathrm{d}\sigma_{\mathrm{C}}(\bar{\epsilon})}{\mathrm{d}\bar{\epsilon}_s \mathrm{d}\bar{\Omega}_s} \tag{3.67}$$

where for $\mathrm{d}\sigma_{\mathrm{C}}(\bar{\epsilon})/\mathrm{d}\bar{\epsilon}_s \mathrm{d}\bar{\Omega}_s$, the expression from (3.65) can be used. The solution of that equation in the $\gamma \gg 1$ is reported as:

$$\frac{d\sigma_{\mathrm{C}}}{d\epsilon_s} \cong \frac{\pi r_e^2}{\gamma\bar{\epsilon}}\,\Xi_{\mathrm{C}}\,H\left(\epsilon_s; \frac{\bar{\epsilon}}{2\gamma}, \frac{2\gamma\bar{\epsilon}}{1 + 2\bar{\epsilon}}\right). \tag{3.68}$$

The function H is the Heaviside step function, equal to 1 between the values defined by $\bar{\epsilon}/2\gamma$ and $2\gamma\bar{\epsilon}/(1+2\bar{\epsilon})$ and zero outside. The Compton kernel is defined as:

$$\Xi_C = y + \frac{1}{y} + \frac{2\epsilon_s}{\gamma\bar{\epsilon}\,y} + \left(\frac{\epsilon_s}{\gamma\bar{\epsilon}\,y}\right)^2 \tag{3.69}$$

where $y = 1 - \epsilon_s/\gamma$ and $\bar{\epsilon_s} = \epsilon\gamma(1-\cos\psi)$, where ψ is the angle between the incident photon and the scattering electron (from equation (3.60)):

$$\cos\psi = \mu\mu_s + \sqrt{1-\mu^2}\sqrt{1-\mu_s^2}\cos\phi \tag{3.70}$$

where we define $\mu \equiv \cos\theta$. The Compton spectral luminosity in the head-on approximation is given by:

$$\epsilon_s L_{\rm C}\left(\epsilon_s, \Omega_s\right) = c\pi r_e^2 \epsilon_s^2 \int_0^{2\pi} d\phi \int_{-1}^{1} d\mu \int_0^{2\epsilon_s/(1-\cos\hat{\psi})} d\epsilon \frac{u(\epsilon,\Omega)}{\epsilon^2} \times \int_{\gamma_{\rm low}}^{\infty} d\gamma N_e\left(\gamma, \Omega_s\right) \Xi_{\rm C}. \tag{3.71}$$

Here, $u(\epsilon,\Omega)$ is the specific energy density of the photon distribution. The value of the lower limit $\gamma_{\rm low}$ of the integration is given by:

$$\gamma_{\rm low} = \frac{\epsilon_s}{2}\left[1 + \sqrt{1 + \frac{2}{\epsilon\epsilon_s(1-\cos\psi)}}\right] \tag{3.72}$$

3.4.4 External Compton

Is it possible for the highly relativistic electrons of the jet to Compton-scatter low energy photon fields of external origin, like the CMB for example, to very high energies. This process is able to explain the intense γ ray radiation coming from the jets of blazars. In order to treat this phenomenon, we are going to follow the approach of Georganopoulos, Kirk, and Mastichiadis [53]. The electron distribution $N_e(\gamma)$ is first transformed to the stationary frame of the target photon density $u(\epsilon,\Omega)$ and then folded with the cross section. By following the aforementioned procedure and then applying equation (3.71) of the head-on approximation, the spectral energy distribution in the received frame coming from a blob is given by:

$$\boxed{\nu F_{\nu}^{\rm EC} = f_{\epsilon_s}^{\rm EC} = \frac{c\pi r_e^2}{4\pi d_L^2}\,\epsilon_s^2\,\delta_D^3 \oint \mathrm{d}\Omega \int_0^{\epsilon_{\rm high}} \mathrm{d}\epsilon\,\frac{u(\epsilon,\Omega;r)}{\epsilon^2} \int_{\gamma_{\rm low}}^{\infty} \mathrm{d}\gamma\,\frac{N_e'(\gamma/\delta_D)}{\gamma^2}\,\Xi_C.} \tag{3.73}$$

3.4.5 Synchrotron Self-Compton

The synchrotron photons emitted by accelerated electrons in the presence of a magnetic field, can get Compton-scattered by the same electrons. In the context of the leptonic models in blazar modelling, this procedure is the origin of the high energy bump of the spectral energy distribution. In order to treat the SSC, Jones's formula (Jones 1968 [54]) of Compton-scattered emissivity for isotropic non-thermal electrons scattering photons of an isotropic external radiation field can be used. Primed quantities are now referring to the emission range (refer to section 3.2.2) of the blob. By taking into account all of the above, we can write the spectral energy distribution of the SSC in the received frame coming from a blob:

$$\boxed{\nu F_{\nu}^{\rm SSC} = f_{\epsilon_s}^{\rm SSC} = \frac{\delta_D^4}{4\pi d_L^2}\,\frac{3}{4} c\,\sigma_\tau \epsilon_s' \int_0^{\infty} \mathrm{d}\epsilon' \frac{u'_{synch}(\epsilon')}{\epsilon'^2} \int_0^{\infty} \mathrm{d}\gamma\,\frac{N_e'(\gamma')}{\gamma'^2}\,F_C(q',\Gamma_e')} \tag{3.74}$$

where

$$u'_{\rm synch} = \frac{3}{4}\,\frac{d_L^2\,f_\epsilon^{\rm synch}}{c\,R_b'^2\,\delta_D^4\,\epsilon'} \tag{3.75}$$

is the specific spectral energy density of the synchrotron photons and $\hat{f}_{\hat{\epsilon}}^{syn}$ is the synchrotron radiation spectrum. The 3/4 term originates from taking the average of the radiation in a sphere. $F_C(q',\Gamma_e')$ is an integration kernel representing the Compton cross section for electrons and photons with a uniform spatial distribution (Jones 1968 [54]; Blumenthal & Gould 1970 [49]):

$$F_C(q',\Gamma_e') = \left[2q'\ln q' + (1+2q')\,(1-q') + \frac{1}{2}\,\frac{(\Gamma_e' q')^2}{1+\Gamma_e' q'}\,(1-q')\right] H\left(q';\frac{1}{4\gamma'},1\right) \tag{3.76}$$

where:

$$\Gamma'_e = 4\epsilon'\gamma', \qquad q' = \frac{\epsilon'/\gamma'}{\Gamma'_e(1-\epsilon'_s/\gamma'}. \tag{3.77}$$

3.5 Absorption of the high-energy radiation

The gamma rays produced in the jet, can interact with low energy photons, in the extra-galactic background light (EBL) for example, and produce electron-positron pairs through the process of $\gamma\gamma$ pair production:

$$\gamma + \gamma \rightarrow e^- + e^+ \tag{3.78}$$

In order to describe the process, first we have to introduce the concept of the invariant mass which characterizes the strength of the collision.

3.5.1 Invariant mass

The invariant mass $\sqrt{s_{\rm tot}}$ is defined as the energy of a system of particles in their center-of-mass frame. In the case of two particles, it is:

$$s_{\rm tot} = (p_1^\mu + p_2^\mu)^2 \tag{3.79}$$

where p_i^μ is the four momentum of the i particle, which is defined as $p_i^\mu = (\epsilon_i/c, \vec{p_i})$ as explained in section 2.2.2. By expanding the parenthesis and using the Minkowski metric for the dot product of the two four-momenta (reference), we get:

$$s_{\rm tot} = \epsilon_1^2 - \vec{p_1}^2 + 2(\epsilon\epsilon_1 - \vec{p}\vec{p_1}) + \epsilon^2 - \vec{p_2}^2 \tag{3.80}$$

where $\epsilon_1 = \sqrt{p_1^2 + m_1^2}$ and $\epsilon = \sqrt{p_2^2 + m_2^2}$ represent the energy of the initial particles and we have set $c = 1$. We use the fact that for ultra-relativistic particles, the mass can be neglected:

$$\epsilon_i^2 = \vec{p_i}^2 + m_i^2 \cong \vec{p_i}^2 \tag{3.81}$$

and therefore, equation (3.80) becomes:

$$s_{\rm tot} = 2(\epsilon\epsilon_1 - \vec{p}\vec{p_1}) \tag{3.82}$$

Which finally results to:

$$s_{\rm tot} = 2\epsilon\epsilon_1(1-\mu) \tag{3.83}$$

where μ is the cosine of the angle (refer to Figure 3.6) between their momenta.

3.5.2 Cross section and optical depth of the $\gamma\gamma$ absorption process

The cross section for $\gamma\gamma$ pair production is obtained from the methods of quantum electrodynamics (Gould, R. J. 2006 [55]; Jauch, J. M. and Rohrlich 1976 [56]) as:

$$\sigma_{\gamma\gamma}(s) = \frac{1}{2}\pi r_e^2 \left(1-\beta_{\rm cm}^2\right)\left[\left(3-\beta_{\rm cm}^4\right)\ln\left(\frac{1+\beta_{\rm cm}}{1-\beta_{\rm cm}}\right) - 2\beta_{\rm cm}\left(2-\beta_{\rm cm}^2\right)\right], \tag{3.84}$$

where we define where $\beta_{\rm cm} = \sqrt{1-s^{-1}} = (1-\gamma_{\rm cm}^{-2})^{1/2}$, and $\sqrt{s} = \gamma_{\rm cm}$ is the center-of-momentum frame Lorentz factor of the produced electron and positron. At threshold, the pair is produced at rest with total energy $2m_ec^2$, so that $s_{\rm tot} = 4$ in units of m_ec^2. Above threshold:

$$s = \gamma_{\rm cm}^2 = \frac{1}{2}\left[\epsilon\epsilon_1(1-\mu)\right] = \frac{s_{\rm tot}}{4}. \tag{3.85}$$

The asymptotes of the cross section are given by:

$$\sigma_{\gamma\gamma}(s) = \pi r_e^2 \begin{cases} \beta_{\rm cm}, & \beta_{\rm cm} \ll 1, \\ \frac{\ln 2s - 1}{s}, & s \gg 1. \end{cases} \tag{3.86}$$

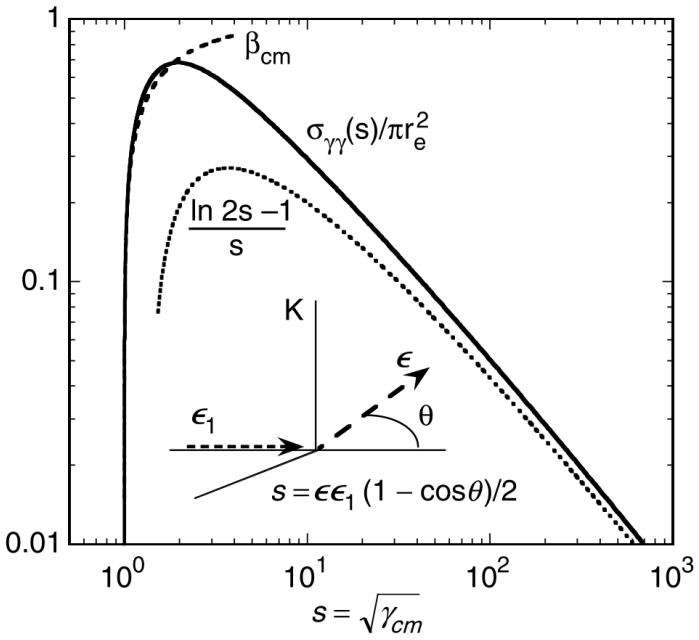

Figure 3.6: **The cross section of the $\gamma\gamma$ absorption**: the cross section as a function of the invariant mass s with the two asymptotes $s - 1 \ll 1$ and $s \gg 1$. The scheme of the collision of the two particles of energies ϵ_1 and ϵ is shown below the curves. [8]

The cross section as a function of the invariant mass is shown in Figure 3.6. When gamma rays interact with isotropic photon fields in head-on collisions, the invariant energy s is approximated by $\epsilon\epsilon_1$ since $\mu = -1$ for $\theta = \pi$. For quick estimates, assuming a typical collision angle of $\theta \cong \pi/2$, s can be approximated by $\epsilon\epsilon_1/2$. However, for reliable estimates, s must be greater than 1, which is the threshold for pair production in $\gamma\gamma$ processes with $\beta_{\rm cm} > 0$ and $\gamma_{\rm cm} > 1$.

To derive a relation for the optical depth, we have to first compute the absorption probability per unit path-length. To do that, we have to consider the scattering rate $\dot{N}_{\rm sc}$ of a photon traversing a photon field. We report the expression:

$$\dot{N}_{\rm sc}\left(\epsilon_1\right) = c \oint d\Omega(1-\mu) \int_0^\infty d\epsilon n_{\rm ph}(\epsilon,\Omega)\sigma\left(\epsilon_r\right). \tag{3.87}$$

The absorption probability per unit path-length is then given by (R.J. Gould and G. P. Schreder 1967 [57]):

$$\frac{d\tau_{\gamma\gamma}\left(\epsilon_1\right)}{dx} = \frac{\dot{N}_{\rm sc}}{c} = \oint d\Omega(1-\mu) \int_0^\infty d\epsilon\, n_{\rm ph}(\epsilon,\Omega)\sigma_{\gamma\gamma}(s), \tag{3.88}$$

and by integrating, we can write the optical depth for the $\gamma\gamma$ absorption for a photon

with dimensionless energy ϵ_1 on a target photon field with number density $n_{\rm ph}$, as:

$$\boxed{\tau_{\gamma\gamma}(\epsilon_1) = \int_0^\infty dx \oint d\Omega(1-\mu) \int_0^\infty d\epsilon \, n_{\rm ph}(\epsilon, \Omega)\sigma_{\gamma\gamma}(s).} \tag{3.89}$$

3.6 Particle distributions

There are four different analytical functions available in order to describe the energy distribution of the electrons in the jet. Since the Lorentz factor γ is used instead of the energy as the variable, the distribution function describes the volume density of the particles in units of cm^{-3} (instead of $\mathrm{cm}^{-3}\,\mathrm{eV}^{-1}$). Apart from the direct definition of its value by the user, it can also be defined by providing the total volume density, the total energy density of the total energy in particles. The available distributions are:

Power law distribution:

$$n(\gamma) = k\,\gamma^{-p} H(\gamma; \gamma_{\rm min}, \gamma_{\rm max}) \tag{3.90}$$

where k is the normalization constant, p the spectral index of the power law and H the Heaviside step function, equal to 1 between the values defined by $\gamma_{\rm max}$ and $\gamma_{\rm min}$, and zero outside.

Broken power law distribution:

$$n(\gamma) = k \left[\left(\frac{\gamma}{\gamma_b}\right)^{-p_1} H(\gamma; \gamma_{\rm min}, \gamma_b) + \left(\frac{\gamma}{\gamma_b}\right)^{-p_2} H(\gamma; \gamma_b, \gamma_{\rm max}) \right] \tag{3.91}$$

where γ_b is the value of the Lorentz factor at which the change in spectral index is occurring and p_1 and p_2 the spectral index before and after the break.

Power law distribution with an exponential cut-off:

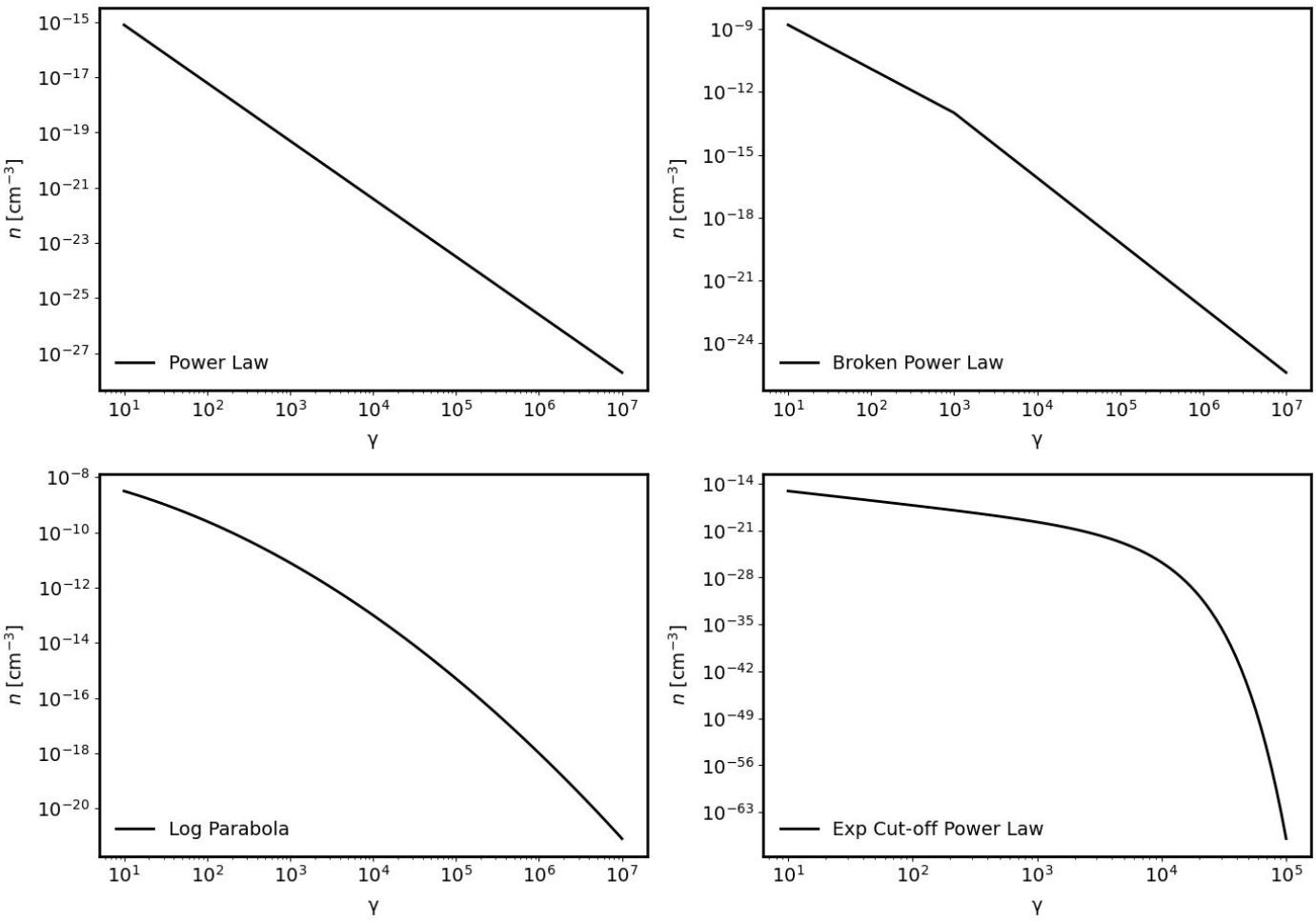

Figure 3.7: **Available particle distributions on `agnpy`:** Power law (upper left panel), Broken power law (upper right panel), Log parabola (lower left panel), Power law with an exponential cut-off (lower right panel).

$$n(\gamma) = k\,\gamma^{-p}\exp\left(-\gamma/\gamma_c\right) H(\gamma;\gamma_{\rm min},\gamma_{\rm max}) \tag{3.92}$$

where γ_c is the value of the Lorentz factor at which the exponential cut-off takes over.

Log-parabolic distribution:

$$n(\gamma) = k\,\left(\frac{\gamma}{\gamma_0}\right)^{-(p+q\log_{10}(\gamma/\gamma_0))} \tag{3.93}$$

where γ_0 is the reference Lorentz factor and q is the spectral curvature. All four distri-

butions are shown in Figure 3.7.

3.7 Towards a lepto-hadronic code for modelling the high-energy emission of jetted AGNs

There are several additions that need to be implemented into `agnpy` in order to evolve to a code capable of lepto-hadronic modelling of the jet. Inside the emission region, apart from the population of the accelerated electrons, there should be the possibility of adding a population of accelerated protons as well. Their acceleration and their interaction with the photon fields would educe all the different hadronic emission processes discussed in section 2.3.2.

In this work, I evolve the open-source `agnpy` package from a fully leptonic to a lepto-hadronic code. I implement two hadronic processes, the proton synchrotron radiation and the photo-meson production process, with the future goal of implementing all the relevant hadronic emission processes. I also implement new particle distribution options to facilitate the comparison with other packages.

CHAPTER 4

Modelling the Hadronic Emission Processes

The broad-band non-thermal emission of jetted AGN cannot always be modelled by leptonic emission processes. Among these examples is the occurrence of orphan flares, an increase in the brightness in just one of the two bumps of the SED. If both bumps originate from the radiation of electrons, they should be correlated with each other. However, the strongest observational evidence in favor of hadronic modelling is the detection of an astrophysical neutrino associated with the flaring blazar TXS 0506+56 in September of 2017.

In this work, two hadronic emission processes are being added to the framework of AGNpy with the aim of providing an alternative to a fully leptonic interpretation: the proton synchrotron radiation and the photomeson process.

In order to validate the correctness of the physical processes I implemented in agnpy, I reproduced results from the literature and, when possible, compared against other (proprietary) modelling software. To expand the range of validations possible with agnpy, I extended the library of analytical models that are available to represent relativistic particles energy distribution. In particular, I introduced the possibility to read and interpolate an arbitrary particle energy distribution produced by the user. This way one can plug to agnpy, for example, a particle distribution produced by another software, e.g. solving the particle kinetic equation.

4.1 Implementation of new particle distributions

The new particle distribution that is being added is an broken power-law with an exponential cut-off. The exponential cut-off makes the distribution more physical than just defining a maximum value for the Lorentz factor (M. Cerruti 2012 [10]). It is a distribution that exists in other packages (such as `Naima` [40]) and therefore it was implemented.

The interpolation function introduced requires as an input the Lorentz factors and the particle densities. The analytical expression of $n(\gamma)$, needed for all the radiative processes calculations, will be given by the function interpolating the set (or array) of values provided by the user. This enables to obtain any density $n(\gamma)$ as long as the value of γ is within the boundaries that were determined by the data.

4.1.1 Interpolation function

The interpolation was done by using the `SciPy` [1] package (Virtanen et al. 2020[37]), an open-source software for mathematics, science and engineering. Specifically, I used the `CubicSpline` interpolator, based on a step-wise cubic polynomial which is continuously differentiable. The `CubicSpline` interpolator calculates the derivative of the interpolated function, which is necessary in order to calculate the Synchrotron Self Absorption (SSA) process. Another simpler tool such as the more commonly used `interp1d` also included in SciPy, for example, doesn't offer this feature.

As energy distribution are commonly provided for log-spaced values of the Lorentz factor, I interpolate the distribution in logarithmic space. Therefore if the interpolation take place in the logarithmic space, the errors will be smaller and the interpolated function will be more accurate. I follow this strategy in the interpolation function.

$$[\gamma, n_\gamma] \xrightarrow[\text{logarithmic space}]{\text{move to}} [\log_{10}\gamma, \log_{10} n_\gamma] \xrightarrow{\text{interpolation}} F_{log}(\log_{10}\gamma) \xrightarrow[\text{linear space}]{\text{move back to}} n(\gamma) = 10^{F_{log}}$$

Calculation of the SSA

We derived the absorption coefficient κ_ν in (3.37). Every particle distribution imple-

[1] https://scipy.org/

mented in the package includes the feature of calculating the integrand of the SSA:

$$\gamma^2 \frac{\mathrm{d}}{\mathrm{d}\gamma}\left(\frac{n(\gamma)}{\gamma^2}\right) \tag{4.1}$$

which is equal to:

$$\frac{\mathrm{d}n(\gamma)}{\mathrm{d}\gamma} - \frac{2n(\gamma)}{\gamma} \ . \tag{4.2}$$

`CubicSpline` is only able to calculate the derivative of the interpolated function in the space that the interpolation took place in. Therefore, it is able to calculate the derivative of $F_{log}(\log_{10}\gamma)$ and not that of $n(\gamma)$. Hence for its calculation, we follow the below steps:

If $u = \log_{10}\gamma$ then:

$$\frac{\mathrm{d}n(\gamma)}{\mathrm{d}\gamma} = \frac{\mathrm{d}10^{F_{log}(u)}}{\mathrm{d}\gamma} = \frac{\mathrm{d}10^{F_{log}(u)}}{\mathrm{d}u} \cdot \frac{\mathrm{d}u}{\mathrm{d}\gamma} \ . \tag{4.3}$$

The first term is:

$$\frac{\mathrm{d}10^{F_{log}(u)}}{\mathrm{d}u} = \ln 10 \cdot 10^{F_{log}(u)} \cdot \frac{\mathrm{d}F_{log}(u)}{\mathrm{d}u} \tag{4.4}$$

while the last one is:

$$\frac{\mathrm{d}u}{\mathrm{d}\gamma} = \frac{\mathrm{d}\log_{10}\gamma}{\mathrm{d}\gamma} = \frac{1}{\gamma \cdot \ln 10} \ . \tag{4.5}$$

Two natural logarithms vanish:

$$\frac{\mathrm{d}10^{F_{log}(u)}}{\mathrm{d}\gamma} = 10^{F_{log}(u)} \cdot \frac{\mathrm{d}F_{log}(u)}{\mathrm{d}u} \cdot \frac{1}{\gamma} \ . \tag{4.6}$$

That is the equation used in the code of the interpolation function, in order to calculate the integrand of the SSA.

Viability of the Interpolation Function

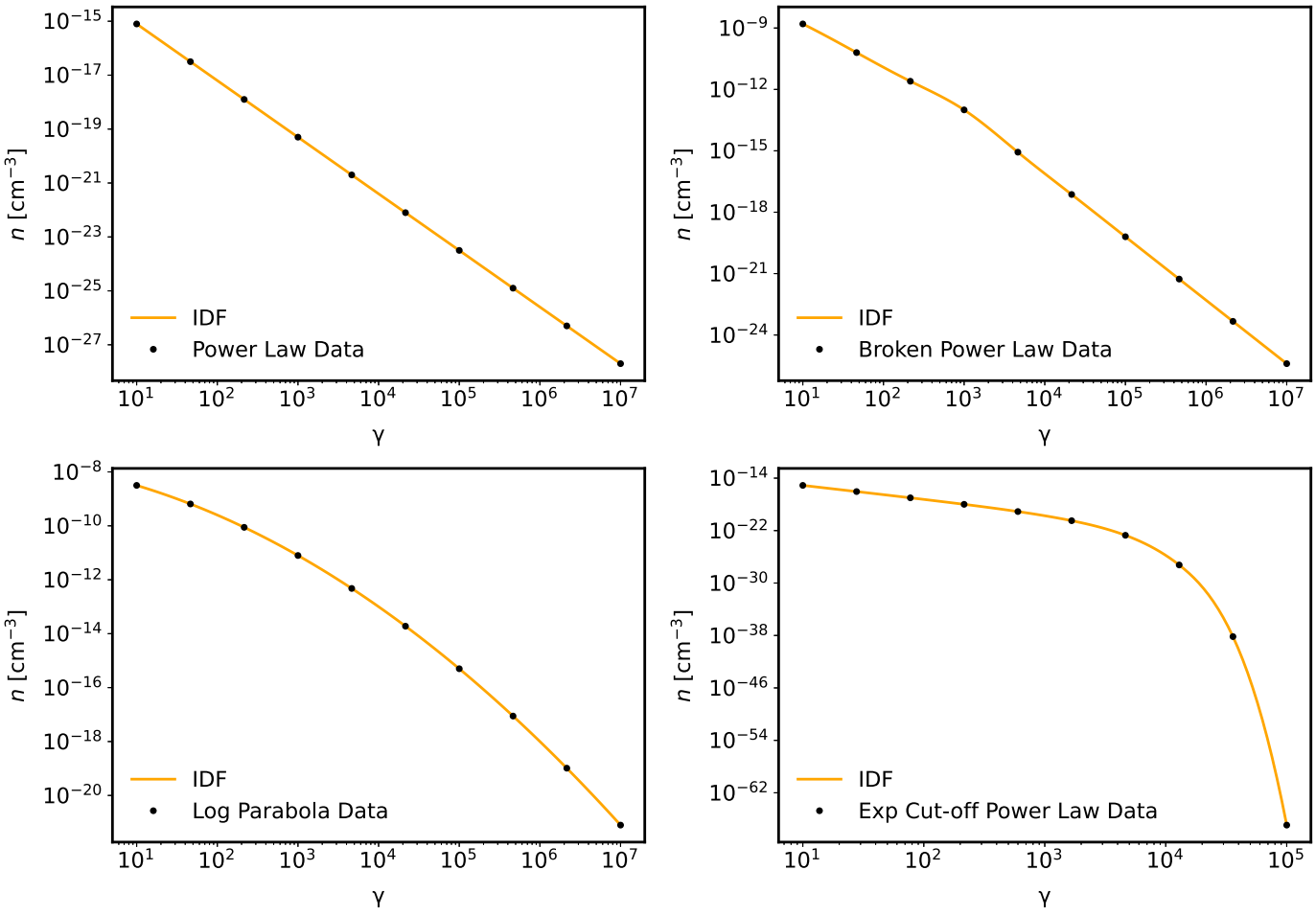

Figure 4.1: **Performance of the interpolation function**: comparison of the input data (bullets) to the outcome of the interpolation for different possible particle distributions (Power law, Broken power law, Log parabola, Power law with an exponential cut-off).

In order to test the viability of the interpolated distribution function (IDF), I produced arrays of energy distributions by evaluating the analytical functions available in agnpy (e.g. power law, refer to section 3.7) over an array of Lorentz factor. I interpolated the density values thus obtained, and verified that the difference between the densities obtained from the interpolated and the original functions were within a given factor. The largest deviation found between the two was smaller than 10^{-6}. The results are reported in Figure 4.1.

The performance of the SSA integrand calculation was also tested. The procedure used was the same and the largest discrepancy found was around 10% for the case of the broken power law. Due to the computation of the derivative, large deviations are to be expected in the case of discontinuities such as breaks in the above case. The results are

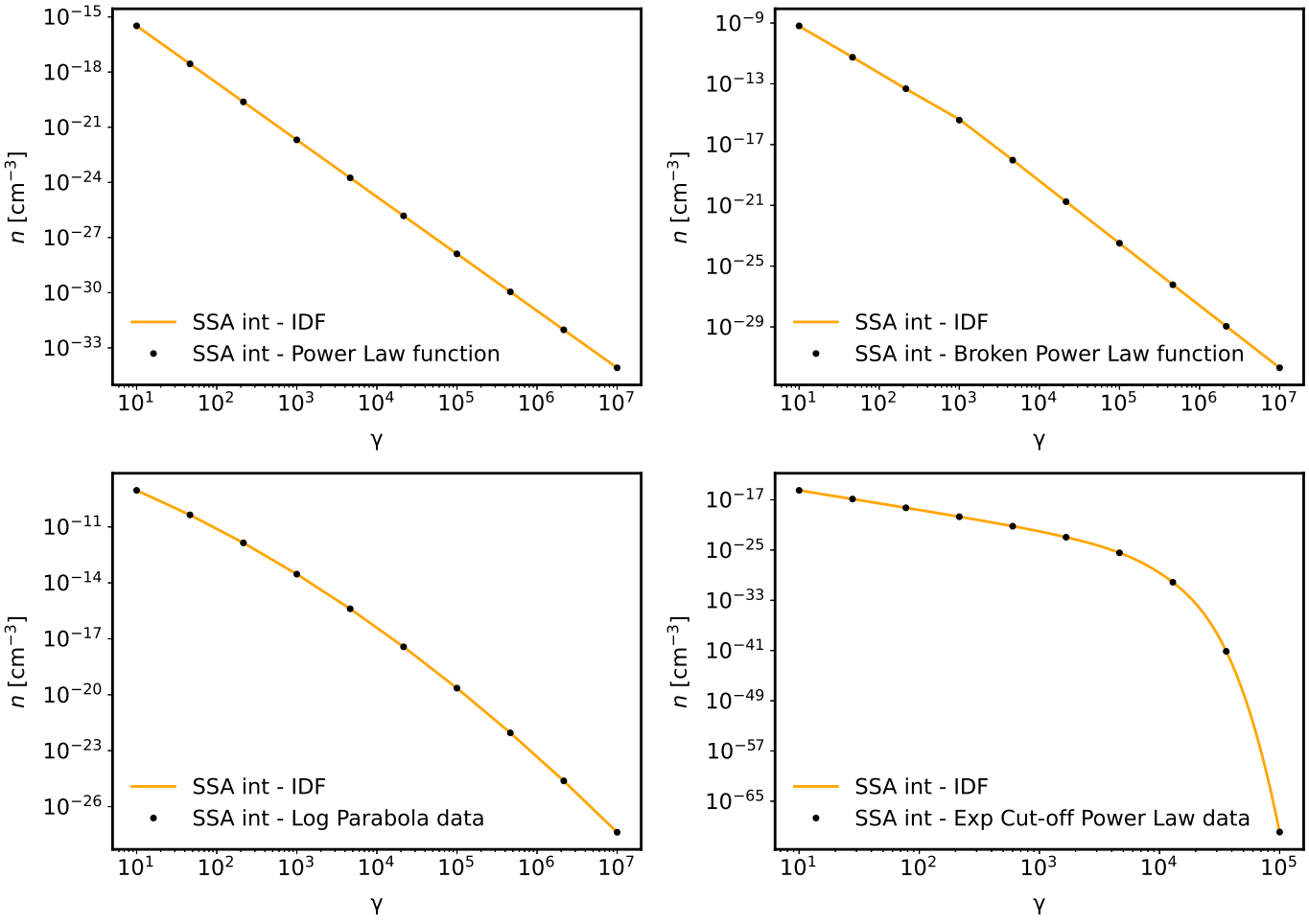

Figure 4.2: **Performance of the interpolation function in calculating the SSA integrand for different particle distributions:** the bullets represent the data used for the interpolation and the line represent the interpolated distribution.

reported in Figure 4.2.

4.1.2 Broken power law with an exponential cut-off

The formula of the broken power law with an exponential cut-off is the following:

$$n(\gamma) = k \left[\left(\frac{\gamma}{\gamma_b} \right)^{-p_1} \exp(-\frac{\gamma}{\gamma_c})\, H(\gamma; \gamma_{\min}, \gamma_b) + \left(\frac{\gamma}{\gamma_b} \right)^{-p_2} \exp(-\frac{\gamma}{\gamma_c}) H(\gamma; \gamma_b, \gamma_{\max}) \right] \tag{4.7}$$

where k is the normalization constant, p_1 and p_2 are the power law indices before

and after the break, γ_b is the Lorentz factor at which the change in spectral index is occurring and γ_{min} and γ_{max} the minimum and maximum values of the Lorentz factor. $H(\gamma; \alpha, \beta)$ function is the Heavinside step function, equal to 1 between the values α and β, and zero outside. An example is shown in Figure 4.3.

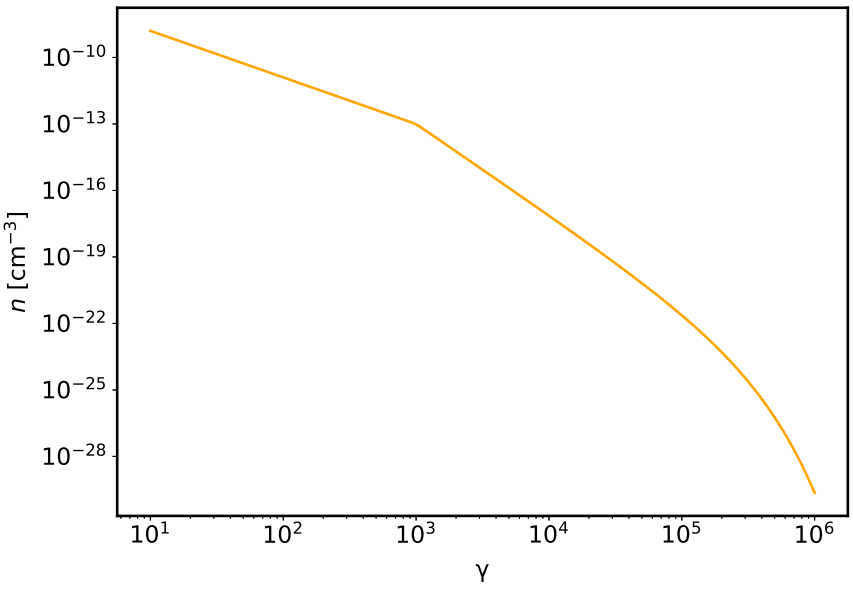

Figure 4.3: **Broken power law with an exponential cut-off** for a random set of parameters.

4.2 Proton synchrotron radiation

In hadronic models, the high-energy component of the spectrum is often described by the synchrotron radiation of accelerated protons. In that case, the synchrotron emission is suppressed in comparison to the case of an identical radiating distribution of electrons, since protons are significantly more massive. In fact, the synchrotron energy losses are proportional to the inverse cube of the mass. Hence, either a considerably stronger magnetic field or a larger particle density (or both) is necessary for their synchrotron radiation to match the luminosity of the high-energy emission that we observe from blazar jets.

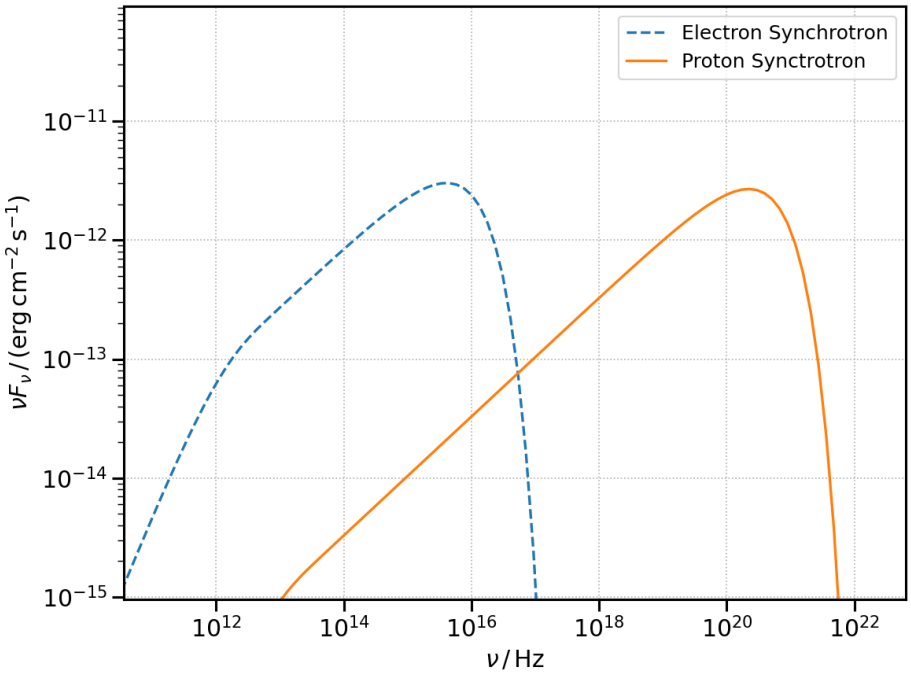

Figure 4.4: **A SED, where the high energy bump is modelled with the radiation from proton synchrotron:** A simple example of a SED, originating from electron and proton synchrotron radiation. The model parameters are shown in Table B.3.

4.2.1 Calculation of the proton synchrotron spectrum

The modelling of the synchrotron radiation was done following exactly the procedure described in section 3.2, but substituting the electron with the proton mass. The synchrotron flux from a relativistic blob with a magnetic field of strength B that consists of an isotropic distribution of protons is given by the expression:

$$\boxed{f_\epsilon^{syn} = \frac{\delta_D^4 \epsilon' J'_{syn}(\epsilon')}{4\pi d_L^2} = \frac{\delta_D^4}{4\pi d_L^2} \frac{\sqrt{3} e^3 B}{h} \epsilon' \int_1^\infty \mathrm{d}\gamma' \, N_\mathrm{p}(\gamma') R(x)} \tag{4.8}$$

where

$$x = \frac{4\pi \epsilon' m_\mathrm{p}^2 c^3}{3eBh\gamma'^2}, \qquad \epsilon' = \frac{h\nu'}{m_\mathrm{p} c^2}. \tag{4.9}$$

where x is derived from $x = \nu/\nu_c$, ν_c is the critical frequency given by (3.12) and ϵ' is the dimensionless energy but instead of the electron rest mass energy, this time the proton rest mass energy is used. The primed quantities refer to the comoving frame

of the blob (the emission reference frame, see section 3.2.2), δ_D is the Doppler factor. The relation between the blob frame and that of the observer is given by (2.50). An example of a SED where the high energy bump is modelled with the proton synchrotron radiation is shown in Figure 4.4.

Synchrotron self absorption was not included in this case, since it affects the lowest energy tail of the spectrum, making its effect undetectable.

4.2.2 Comparison with other packages

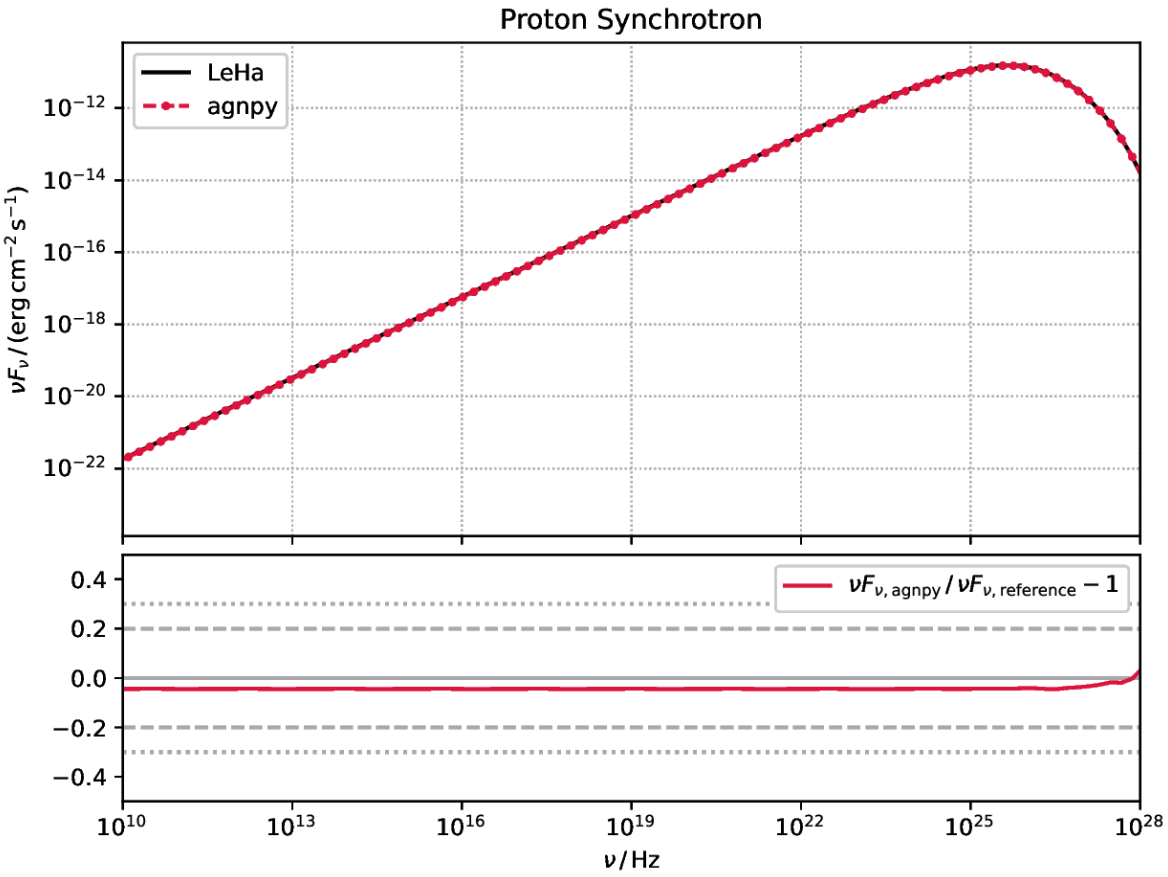

Figure 4.5: **Comparison of the SED of the proton synchrotron radiating as calculated from `agnpy` and the `LeHa-Paris` code**: In the bottom panel, the deviation of `agnpy` with the `LeHa-Paris` code is demonstrated with the quantity $(\nu F_{\nu,\mathrm{agnpy}}/\nu F_{\nu,\mathrm{ref}}) - 1$. The model parameters are shown on Table B.2.

In order to validate the proton synchrotron model, I cross-checked the results with the `LeHa-Paris` code (Cerruti et al. 2012 [35]). The `LeHa-Paris` code is a well-established tool with a proven track record in computing the steady-state emission of photons and neutrinos. Like `agnpy`, it is a steady-state code that approximates the emission region

of the high-energy radiation of the jet with a spherical plasmoid, therefore making it the appropriate code to test my results.

In order to carry out the comparison, the proton synchrotron spectrum was generated with both codes, using the same exact proton distribution and blob parameters, on which we observe a small deviation of less than 5%. In Figure 4.5, the comparison of the two models is demonstrated. In the bottom panel, the deviation of `agnpy` with the `LeHa-Paris` code is demonstrated with the quantity $(\nu F_{\nu,\mathrm{agnpy}}/\nu F_{\nu,\mathrm{ref}}) - 1$.

4.3 Implementation of the photo-meson production

One of the mechanisms considered for particle production and radiation in high-energy astrophysical sources is the so-called photo-meson production, indicating the interaction of an ultra-relativistic proton, typically accelerated in a source, with a low-energy photon from the source environment. It results into the creation of neutral and charged pions that eventually leads into the emission of γ-ray, leptons but most importantly, neutrinos (refer to section 2.3.2 for a more complete description).

For the implementation of the process, I followed F.R Kelner and F.R.Aharonian 2008 [12]. They provide simple analytical parametrizations for the energy distributions of the decay products by running a large number of simulations of the `SOPHIA` code (Mücke et al. 2000 [58]) and producing a fitting function of the results. The main drawback from such approach is that the intermediate particles (pions and muons) are being integrated out and therefore their cooling can not be described. The final decay products of which the spectra are calculated are photons, electrons, positrons and neutrinos.

4.3.1 Analytical treatment of the photo-meson production

Following F.R Kelner and F.R.Aharonian 2008 [12], the spectrum of each decay particle is given by the following expression, in units of $\mathrm{cm}^{-3}\,\mathrm{s}^{-1}$:

$$\frac{dN}{dE} = \int_{\eta_0}^{\infty} H(\eta, E)\, d\eta \tag{4.10}$$

where $H(\eta, E)$ is given by:

$$H(\eta, E) = \int_E^\infty \frac{dE_\mathrm{p}}{E_\mathrm{p}^2} f_\mathrm{p}(E_\mathrm{p})\, f_{ph} \left(\eta \frac{m_\mathrm{p}^2 c^4}{4E_\mathrm{p}}\right) \Phi_i \left(\eta, \frac{E}{E_\mathrm{p}}\right) \tag{4.11}$$

and η is given by:

$$\eta = \frac{4\epsilon E_\mathrm{p}}{m_\mathrm{p}^2 c^4}. \tag{4.12}$$

E_p is the proton energy, ϵ is the energy of the target photon, E the energy of the output product, and f_p and f_{ph} are the energy distributions of the protons and the soft photons. The value of $\eta = \eta_0$ characterizes the threshold of the interaction and it is equal to about 0.313.

$\Phi_i(\eta, E/E_\mathrm{p})$ is a characteristic function that differs for each decay product and essentially contains the information of the kinematics and the cross sections. Its analytical form is obtained by numerical results of simulations of the `SOPHIA` code and it reads as follows:

If $x = E/E_\mathrm{p}$, then in the range $x_- < x < x_+$:

$$\Phi_i(\eta, x) = B_i \exp\left\{-s_i \left[\ln\left(\frac{x}{x_-}\right)\right]^{\delta_i}\right\} \left[\ln\left(\frac{2}{1+y^2}\right)\right]^{\psi} \tag{4.13}$$

where $y = (x - x_-)/(x_+ - x_-)$, while at low energies, $x < x_-$:

$$\Phi_i(\eta, x) = B_i (\ln 2)^{\psi}. \tag{4.14}$$

In the case of $x > x_+$, then simply the $\Phi_i(\eta, x)$ is equal to zero. The index i indicates the type of the final product and can be either γ in the case of the gamma rays produced from the π^0 decay or l in the case of the produced leptons.

The parameters B_i, s_i and δ_i are functions of η with their values depending on the type of the product particle. The x_- and x_+ are the maximum and minimum energies of each output particle and they differ depending on its type, and along with the power index ψ, are as well functions of η. The specific expressions of these limits, the power law index and the tables of the constants B_i, s_i and δ_i can be found at the reference paper ([12]).

4.3.2 Limitations of the photo-meson production calculation

The main drawback from such approach is that the intermediate particles (pions and muons) are being integrated out, meaning that they are considered to decay instantly, producing the photons, neutrinos and leptons. Therefore the cooling can not being described. It has been shown that their emission can be significant in some specific cases to the high-energy spectrum, in models where proton synchrotron is the dominant process for the high-energy bump of the SED as demonstrated by Mücke et al. 2003 [59]. Therefore, while this particular theoretical method is valid, it should only be employed if at least one of the certain conditions are met to ensure that neglecting the cooling of the secondaries is not an issue. One of the two conditions must be fulfilled, as stated by Böttcher et al. 2013 [11]:

1. The synchrotron cooling time of pions and muons is much larger than their decay time scales, which yields the condition:

$$B\gamma_p \ll \begin{cases} 7.8 \times 10^{11}\mathrm{G} & \text{for pions} \\ 5.6 \times 10^{10}\mathrm{G} & \text{for muons} \end{cases} . \tag{4.15}$$

   where γ_p is the Lorentz factor of protons and B the magnetic field's strength.

2. The proton synchrotron energy losses strongly dominate over photo-pion losses.

4.3.3 Comparison with the literature

The reference paper presents several plots of spectra for the output neutrinos, leptons, and photons that result from the interaction between the CMB radiation field and different proton distributions. These spectra can be utilized to validate the precision of the code.

The proton distribution used in the reference paper to produce the spectra was a power law with exponential cut-off. There are four examples in total, where the cut-off energies are $E_\mathrm{cut} = 0.01, 0.1, 1, 1000 \cdot E_*$, where E_* is the characteristic energy of the proton, defined as:

$$E_* = m_p c^2 \left(\frac{m_p c^2}{4kT} \eta_0 \right) \approx 3.0 \times 10^{20}\mathrm{eV} \tag{4.16}$$

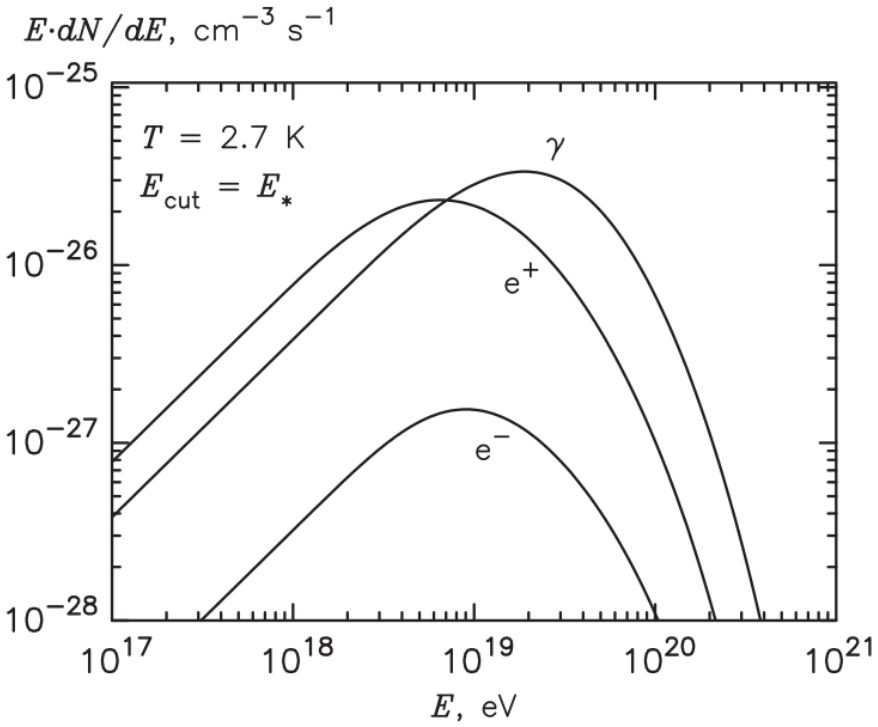

Figure 4.6: **Example presented in the reference paper of photon and lepton spectra produced by the photomeson production:** Left panel of Figure 15 from [12] displays the output spectra of photons, positrons, and electrons generated by a proton distribution modeled as a power law with an exponential cut-off at $E_{\rm cut} = E_*$, interacting with the CMB radiation field as the soft photon distribution.

A proton with this energy and a photon of energy kT can produce a pion thought a head-on collision. The power law with the exponential cut-off is given by the expression:

$$f_{\rm p}(E_{\rm p}) = A{E_{\rm p}}^{-2} \exp\left(-\frac{E_{\rm p}}{E_{\rm cut}}\right) \tag{4.17}$$

where the normalization constant is determined from the condition:

$$\int_{1\,\mathrm{GeV}}^{\infty} E_{\rm p} J_{\rm p}(E_{\rm p}) \mathrm{d}E_{\rm p} = 1 \frac{\mathrm{erg}}{\mathrm{cm}^3} \tag{4.18}$$

For the purpose of this section, I focus on demonstrating examples with cut-off energies of $E_{\rm cut} = E_*$ and $E_{\rm cut} = 1000 \cdot E_*$. Comparison plots of the cases where $E_{\rm cut} = 0.1 \cdot E_*$ and $E_{\rm cut} = 10 \cdot E_*$ are included in the Appendix A.

In the case of $E_{\rm cut} = E_*$, Figures 4.6 and 4.7, the output spectra of the reference paper are presented when $E_{\rm cut} = E_*$. To compare these results with those generated by my

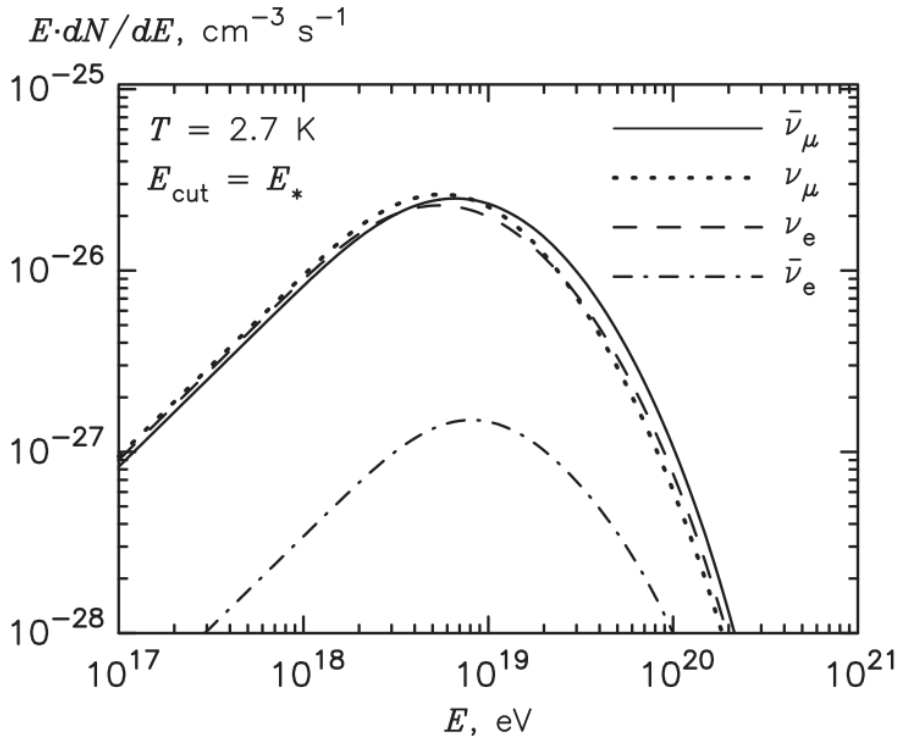

Figure 4.7: **Example presented in the reference paper of neutrino spectra produced by the photomeson production:** Right panel of Figure 15 from [12] displays the output spectra of neutrinos and leptons generated by a proton distribution modeled as a power law with an exponential cut-off at $E_{\rm cut} = E_*$, interacting with the CMB radiation field as the soft photon distribution.

code, I extracted points from these plots and plotted them in Figures 4.8 and 4.9. I found that the largest deviation between the reference paper and the code was around 10%, while in most cases less than 5%. A good agreement was also observed in the other two cases, where the cut-off energy was set to $0.1 \cdot E_*$ and $10 \cdot E_*$ (refer to Appendix A).

When $E_{\rm cut}$ is equal to $1000 \cdot E_*$, a discrepancy larger than 20% between my code and the reference paper emerges beyond 10^{20} eV, as shown in Figure 4.10. This implies that probably there is an issue with the integration method I used in the calculation of the integral of equation (4.11). It should be noted, however, that a proton distribution with such high energies is not physically feasible, as far as our current understanding goes. In addition, as we discussed in the subsection 4.3.2, the modelling itself is not valid for cases with such energetic protons, since condition (4.15) must be met.

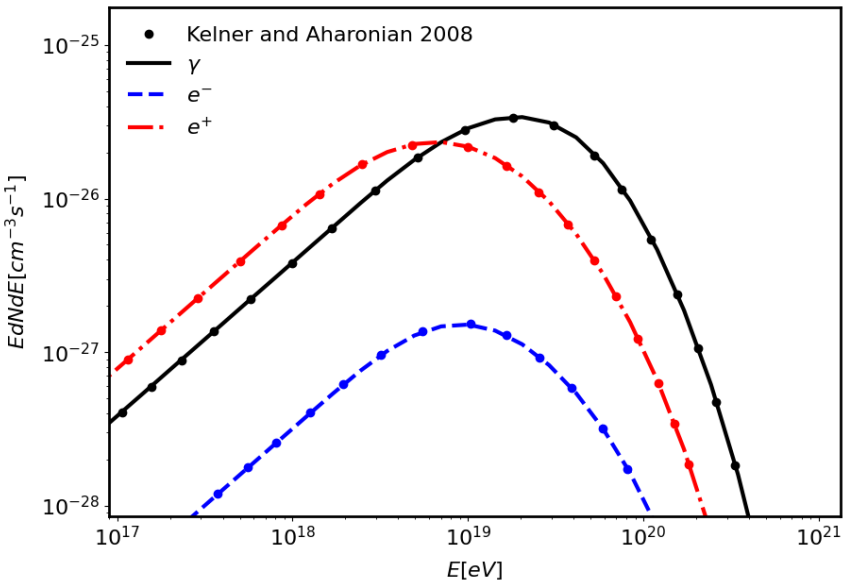

Figure 4.8: **Comparison of the output spectra of photons and leptons generated from the code and those of the reference paper**: The proton distribution is a power law with an exponential cut-off at $E_{\rm cut} = E_*$, while the soft photon distribution is the CMB radiation field.

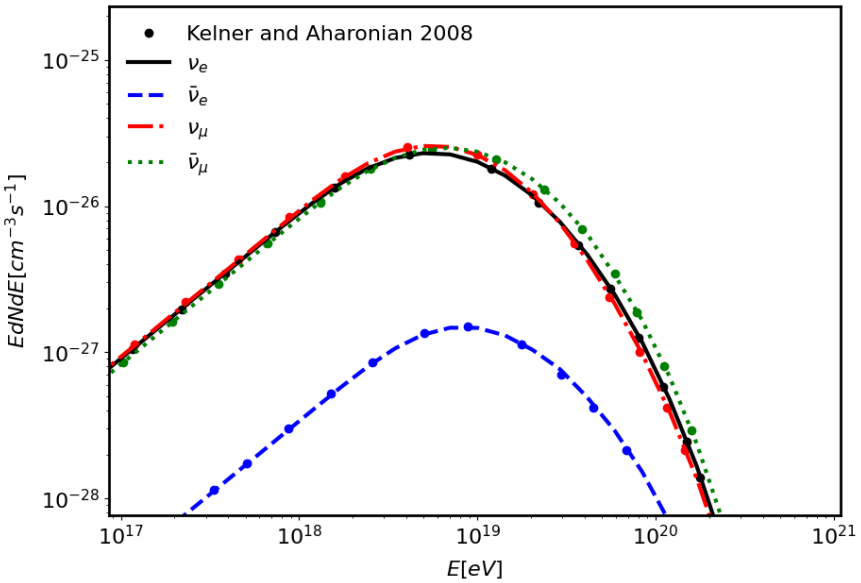

Figure 4.9: **Comparison of the output spectra of neutrinos generated from the code and those of the reference paper**: The proton distribution is a power law with an exponential cut-off at $E_{\rm cut} = E_*$, while the soft photon distribution is the CMB radiation field.

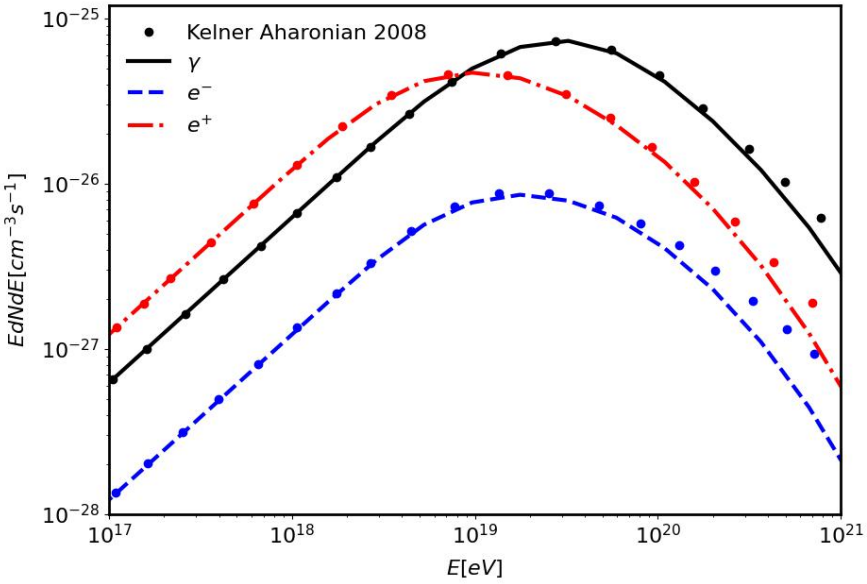

Figure 4.10: **Comparison of the output spectra of photons and leptons generated from the code and those of the reference paper**: The proton distribution is is a power law with an exponential cut-off at $E_{\rm cut} = 1000 \cdot E_*$, while the soft photon distribution is the CMB radiation field. The discrepancy starts at around 10^{20} eV, however a proton distribution with such high energies is not physically feasible.

4.3.4 Modelling the emission region of the photomeson process as a blob in the jet

The objective of this thesis is to model the hadronic emission processes occurring within the emission region of the jet, which I approximate as a uniform spherical blob (in the comoving frame). Therefore, the according relativistic transformations have to be applied in order to obtain the SED as seen by the observer. As we have seen in section 2.2.3, the SED of a relativistic blob is given by the expression:

$$f_\epsilon = \frac{\delta_{\rm D}^4}{4\pi d_L^2} V_b' \epsilon' j'(\epsilon') \tag{4.19}$$

where primed quantities refer to the comoving frame.

Observed SED of photons and neutrinos

I treat neutrinos as photons, since the upper limit of their mass equal to 0.8 eV/c^2 (KATRIN collaboration 2022 [60]) results to a very small and hence, negligible error in the calculation of their spectrum.

In case of neutrinos and photons produced from the photomeson process, the emissivity is given by:

$$V'_b\,\epsilon'\,j'(\epsilon') = V'_b\left(E'^2\,\frac{\mathrm{d}N}{\mathrm{d}E'}\right) = V'_b\,\left(\epsilon'^2\,m_{\mathrm{p}}^2c^4\frac{\mathrm{d}N}{\mathrm{d}E'}\right) \tag{4.20}$$

where $\mathrm{d}N/\mathrm{d}E'$ is the photon or neutrino spectrum, given by (4.10) in units of $\mathrm{eV}^{-1}\,\mathrm{cm}^{-3}\,\mathrm{s}^{-1}$ and the dimensionless energy is given by:

$$\epsilon' = \frac{E'}{m_{\mathrm{p}}c^2} = \frac{h\nu'}{m_{\mathrm{p}}c^2}. \tag{4.21}$$

Therefore, the spectral energy distribution in the case of photons and neutrinos is given by:

$$\boxed{f_\epsilon^{p\gamma} = \frac{\delta_D^4}{4\pi d_L^2}V'_b\epsilon' j'(\epsilon') = \frac{\delta_D^4}{4\pi d_L^2}\,V'_b\,\left(\epsilon'^2\,m_{\mathrm{p}}^2c^4\,\frac{\mathrm{d}N}{\mathrm{d}E'}\right)} \tag{4.22}$$

Figure (4.11) displays the spectra of the produced photons and some of the produced neutrinos. The proton distribution is modeled as a power law with an exponential cut-off, limited to energies below the thresholds specified in section 4.3.2, while the soft photon distribution is an arbitrary non-thermal distribution, described by a simple power law.

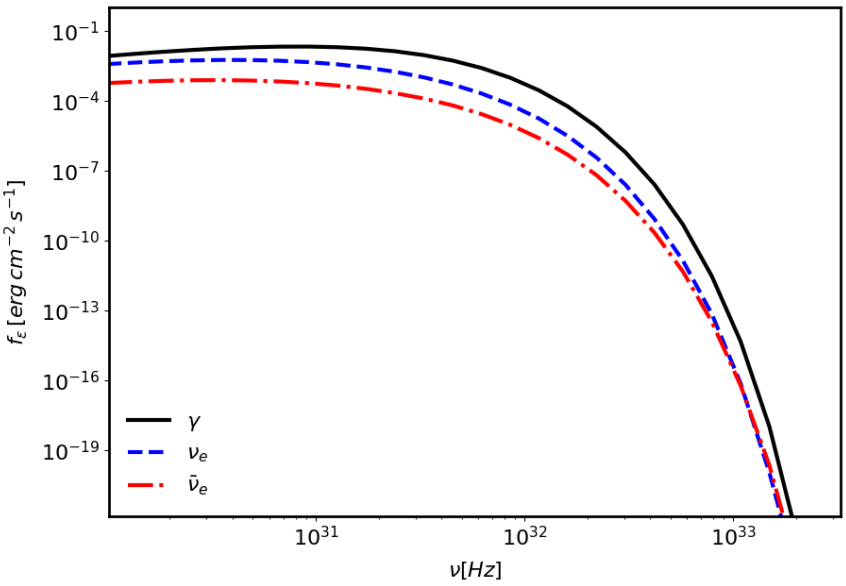

Figure 4.11: **The SED of the produced photons, electron neutrinos and electron anti-neutrinos, from the photomeson process:** The proton distribution is modeled as a power law with an exponential cut-off, limited to energies below the thresholds specified in section 4.3.2, while the soft photon distribution is an arbitrary non-thermal distribution, described by a simple power law. Model parameters are shown in Table B.3.

CHAPTER 5

Conclusions and Future Prospects

The objective of this thesis was the development of an open-source code for modeling the leptonic and hadronic emission processes that occur in the relativistic jets of blazars. To accomplish this, I incorporated the proton synchrotron radiation and the photo-meson production in the python package `agnpy`.

In the context of hadronic modelling, proton synchrotron radiation can dominate the flux of the second high-energy bump of the SED, when a powerful magnetic field is present. It was modelled following the approach of Dermer & Menon 2009 [8] and Finke et al. 2008 [44]. I compared the model with the `LeHa-Paris` code and found excellent agreement between the two models, with a discrepancy of less than 5%.

The process of photo-meson production is the primary source of neutrinos in blazars, with proton-proton interactions only becoming relevant in the event of the jet encountering a target, such as a gas cloud or a star. I was able to effectively model the photo-meson production by using analytical parametrizations of the energy distributions of decay products based on the work of F.R Kelner and F.R.Aharonian in 2008 [12]. My results were compared with examples presented in the paper, and an excellent agreement with discrepancies less than 5% in most cases. However, a discrepancy of 20% emerged for proton distributions at energies up to 10^{24} eV, yet it should be noted that such energies are not physically feasible and greatly surpass the maximum energies

that protons can attain.

Further development is required for the code to incorporate other relevant hadronic processes. The implementation of the Bethe-Heitler pair production, a process which is in competition with the photo-meson production, is crucial. Even thought the latter dominates the radiative output for interactions of high-energy protons with photons, the Bethe-Heitler process is the main proton-photon interaction channel for low energy protons.

In addition, pair cascades originating from both the photo-meson and the Bethe-Heitler processes should be considered as well. The photons generated by pion decay during photo-meson interactions, as well as the synchrotron and inverse Compton emissions from secondary electron-positron pairs, arise in an energy range where the dense soft radiation fields in the emission region are opaque to $\gamma\gamma$ pair production. Consequently, these secondary products of photohadronic processes trigger an electromagnetic cascade upon interacting with the soft photon fields.

Finally, proton-proton interactions gain relevance whenever there is a significant particle density, higher than that of the soft photon field, which is the case for galactic sources like supernova remnants. In the case of the relativistic jets of blazars where the jet plasma has a very low density, these interactions only become significant when the jet collides with a target, such as a gas cloud or a star. Although the importance of proton-proton interactions may not be as pronounced as that of the previously mentioned processes, their inclusion in the code will make it complete.

Before this work, the python package `agnpy` was able to model the spectral energy distribution of blazars through just leptonic emission models. However now, by implementing the proton synchrotron radiation and the photo-meson process, `agnpy` will be the first open-source package that includes hadronic processes for the modelling of the high-energy emission of jetted active galactic nuclei. It will be accessible to the wider scientific community, regardless of institutional or financial constraints.

APPENDIX A

Additional plots

In section 4.3.3, we compared `agnpy` to the reference paper [12]. The examples presented examined cases where the exponential cut-off of the proton distribution equaled either $E_{\rm cut} = 1, 1000 \cdot E_*$, where $E_* = 3 \cdot 10^{20}$ represents the characteristic energy of the protons. This appendix showcases the remaining two examples, which plot for $E_{\rm cut} = 0.1, 10 \cdot E_*$. The plotted points represent the reference paper, while the lines represent the output of `agnpy`.

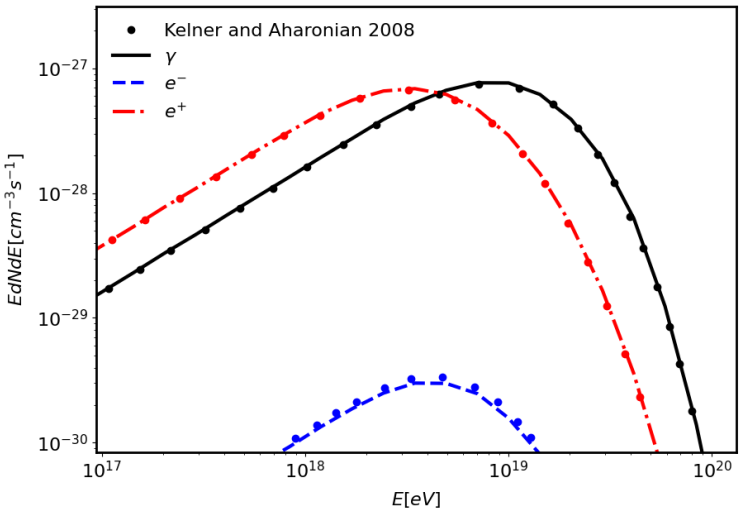

Figure A.1: **Comparison of the output spectra of photons and leptons generated from the code and those of the reference paper**: The proton distribution is a power law with an exponential cut-off at $E_{\text{cut}} = 0.1 \cdot E_*$, while the soft photon distribution is the CMB radiation field.

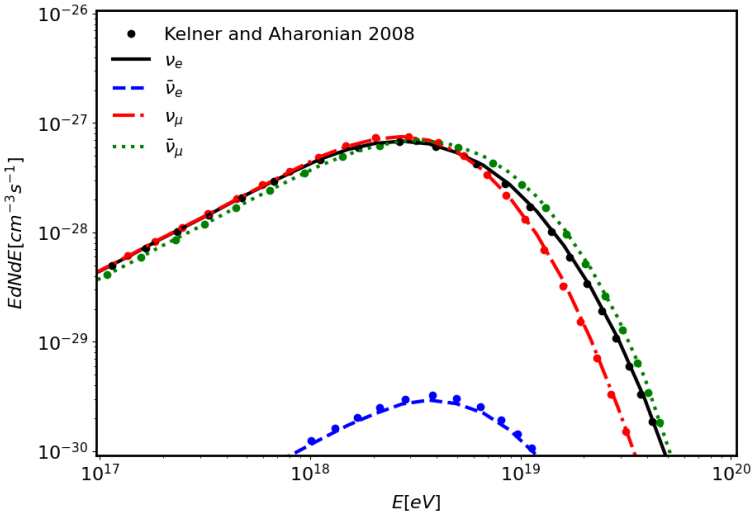

Figure A.2: **Comparison of the output spectra of neutrinos generated from the code and those of the reference paper**: The proton distribution is a power law with an exponential cut-off at $E_{\text{cut}} = 0.1 \cdot E_*$, while the soft photon distribution is the CMB radiation field.

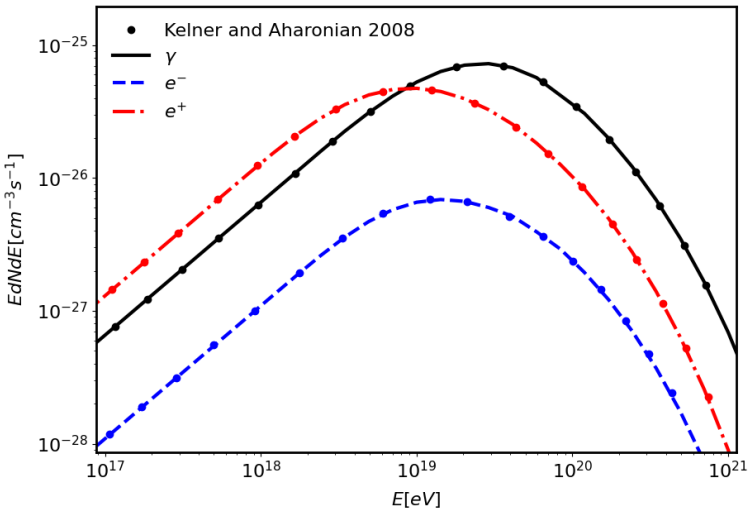

Figure A.3: **Comparison of the output spectra of photons and leptons generated from the code and those of the reference paper**: The proton distribution is a power law with an exponential cut-off at $E_{\rm cut} = 10 \cdot E_*$, while the soft photon distribution is the CMB radiation field.

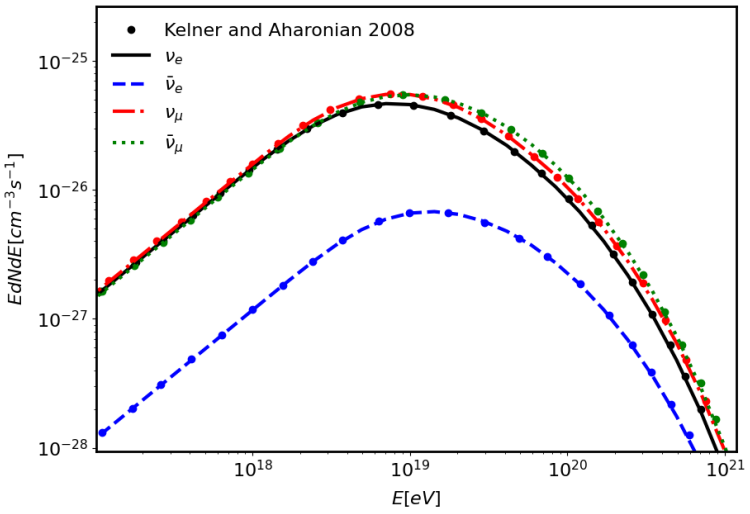

Figure A.4: **Comparison of the output spectra of neutrinos generated from the code and those of the reference paper**: The proton distribution is a power law with an exponential cut-off at $E_{\rm cut} = 10 \cdot E_*$, while the soft photon distribution is the CMB radiation field.

APPENDIX B

Tables

Blob	Values	Proton distribution n_p	Values	Electron distribution n_e	Values
B [G]	1	k [cm^{-3}]	3000	k [cm^{-3}]	10
z	0.1	p	2.0	p	2.0
δ_D	30	γ_min	10^4	γ_min	10^2
Γ	16	γ_max	10^8	γ_max	10^4
R [cm]	10^{16}	-	-	-	-

Table B.1: **Parameters used in Figure 4.4**: Both the proton distribution n_p and the electron distribution n_e are described by simple power laws.

Blob	Values	Proton distribution n_p	Values
B [G]	62.8936	k [cm^{-3}]	21009
z	0.44	p_1	1.5
δ_D	30	p_2	2.5
Γ	15	γ_b	$3.64 \cdot 10^9$
R [cm]	$9.062 \cdot 10^{14}$	γ_c	$3.64 \cdot 10^9$
-	-	γ_min	10^4
-	-	γ_max	10^8

Table B.2: **Parameters used in Figure 4.5**: The proton distribution n_p is described by a broken power law with an exponential cut-off.

Blob	Values	Proton distribution n_{p}	Values	Soft photon distribution f_{ph}	Values
B [G]	80	k [cm^{-3}]	28.26	norm [cm^{-3}]	10^{-5}
z	0.117	p	2.0	p	2.0
δ_D	30	γ_c	10^7	-	-
Γ	16	γ_{min}	10^3	-	-
R [cm]	$5.2 \cdot 10^{14}$	γ_{max}	10^9	-	-

Table B.3: **Parameters used in Figure 4.11**: The proton distribution n_{p} is described by a power law with an exponential cut-off, while the soft photon distribution by a simple power law.

Acknowledgments

I want to thank Elisa Bernardini for introducing me to this field, for being my supervisor and for helping me to organize my thoughts. She genuinely cared about my well-being and very often reminded me to take care of myself. She is an honest person who deeply cares about her students.

I want to thank Cosimo Nigro for allowing me to undertake my thesis while working as a developer on agnpy. He was consistently available to discuss the next steps and to patiently explain how to proceed with the code always with a smile.

Last but certainly not least, I want to thank Ilaria Viale. We went thought this together, from the *how to use git* tutorials to contributing to agnpy. She guided me throughout the thesis and was always there to calm me down when things were not looking good. Finally, for patiently opening for me the door of the office after the same exact text message every morning: "Ciao potresti aprirmi, sono fuori".

Bibliography

[1] C Megan Urry and Paolo Padovani. Unified schemes for radio-loud active galactic nuclei. *Publications of the Astronomical Society of the Pacific*, 107(715):803, 1995.

[2] Bradley W Carroll and Dale A Ostlie. *An introduction to modern astrophysics*. Cambridge University Press, 2017.

[3] Walter Jaffe, Holland C Ford, Laura Ferrarese, Frank van den Bosch, and Robert W O'Connell. A large nuclear accretion disk in the active galaxy ngc4261. *Nature*, 364:213–215, 1993.

[4] Volker Beckmann and Chris Shrader. *Active galactic nuclei*. John Wiley & Sons, 2012.

[5] Chiara Righi and Fabrizio Tavecchio. *Neutrino emission from Blazars*. PhD thesis, Università degli Studi dell'Insubria, 2019.

[6] M Landoni, R Falomo, A Treves, B Sbarufatti, M Barattini, R Decarli, and J Kotilainen. Eso very large telescope optical spectroscopy of bl lacertae objects. iv. new spectra and properties of the full sample. *The Astronomical Journal*, 145(4):114, 2013.

[7] Gabriele Ghisellini, Chiara Righi, L Costamante, and Fabrizio Tavecchio. The fermi blazar sequence. *Monthly Notices of the Royal Astronomical Society*, 469(1):255–266, 2017.

[8] Charles D Dermer and Govind Menon. *High energy radiation from black holes: gamma rays, cosmic rays, and neutrinos*, volume 17. Princeton University Press, 2009.

[9] George B Rybicki and Alan P Lightman. *Radiative processes in astrophysics*. John Wiley & Sons, 1991.

[10] Matteo Cerruti. *High-Energy emission from Active Galactic Nuclei*. PhD thesis, Université de Paris 7-Denis Diderot, 2012.

[11] M Böttcher, A Reimer, K Sweeney, and A Prakash. Leptonic and hadronic modeling of fermi-detected blazars. *The Astrophysical Journal*, 768(1):54, 2013.

[12] SR Kelner and FA Aharonian. Energy spectra of gamma rays, electrons, and neutrinos produced at interactions of relativistic protons with low energy radiation. *Physical Review D*, 78(3):034013, 2008.

[13] Charles Messier. Catalogue des nébuleuses et des amas d'étoiles (catalog of nebulae and star clusters). *Connoissance des Temps ou des Mouvements Célestes*, pages 227–267, 1781.

[14] Carl K Seyfert. Nuclear emission in spiral nebulae. *The Astrophysical Journal*, 97:28, 1943.

[15] Maarten Schmidt. 3 c 273: a star-like object with large red-shift. *Nature*, 197(4872):1040–1040, 1963.

[16] Juhan Frank, Andrew King, and Derek Raine. *Accretion power in astrophysics*. Cambridge university press, 2002.

[17] JRP Angel and HS Stockman. Optical and infrared polarization of active extragalactic objects. *Annual Review of Astronomy and Astrophysics*, 18(1):321–361, 1980.

[18] P Padovani and CM Urry. Luminosity functions, relativistic beaming, and unified theories of high-luminosity radio sources. *Astrophysical Journal, Part 1 (ISSN 0004-637X), vol. 387, March 10, 1992, p. 449-457.*, 387:449–457, 1992.

[19] Bernard L Fanaroff and Julia M Riley. The morphology of extragalactic radio sources of high and low luminosity. *Monthly Notices of the Royal Astronomical Society*, 167(1):31P–36P, 1974.

[20] G al Fossati, L Maraschi, A Celotti, A Comastri, and G Ghisellini. A unifying view of the spectral energy distributions of blazars. *Monthly Notices of the Royal Astronomical Society*, 299(2):433–448, 1998.

[21] Gabriele Ghisellini. The blazar sequence 2.0. *Galaxies*, 4(4):36, 2016.

[22] Alan P Marscher and Walter Kieran Gear. Models for high-frequency radio outbursts in extragalactic sources, with application to the early 1983 millimeter-to-infrared flare of 3c 273. *Astrophysical Journal, Part 1 (ISSN 0004-637X), vol. 298, Nov. 1, 1985, p. 114-127.*, 298:114–127, 1985.

[23] G Ghisellini, L Maraschi, and A Treves. Inhomogeneous synchrotron-self-compton models and the problem of relativistic beaming of bl lac objects. *Astronomy and Astrophysics*, 146:204–212, 1985.

[24] A Konigl. Relativistic jets as x-ray and gamma-ray sources. *The Astrophysical Journal*, 243:700–709, 1981.

[25] Susumu Inoue and Fumio Takahara. Electron acceleration and gamma-ray emission from blazars. *The Astrophysical Journal*, 463:555, 1996.

[26] K Katarzyński, H Sol, and A Kus. The multifrequency emission of mrk 501-from radio to tev gamma-rays. *Astronomy & Astrophysics*, 367(3):809–825, 2001.

[27] Marek Sikora, Mitchell C Begelman, and Martin J Rees. Comptonization of diffuse ambient radiation by a relativistic jet: The source of gamma rays from blazars? *The Astrophysical Journal*, 421:153–162, 1994.

[28] Hughes Krawczynski, SB Hughes, D Horan, F Aharonian, MF Aller, H Aller, P Boltwood, J Buckley, P Coppi, G Fossati, et al. Multiwavelength observations of strong flares from the tev blazar 1es 1959+ 650. *The Astrophysical Journal*, 601(1):151, 2004.

[29] Markus Böttcher. A hadronic synchrotron mirror model for the "orphan" tev flare in 1es 1959+ 650. *The Astrophysical Journal*, 621(1):176, 2005.

[30] Sarira Sahu, Andres Felipe Osorio Oliveros, and Juan Carlos Sanabria. Hadronic-origin orphan tev flare from 1es 1959+ 650. *Physical Review D*, 87(10):103015, 2013.

[31] MG Aartsen, M Ackermann, and J Adams. 2018b. multimessenger observations of a flaring blazar coincident with high-energy neutrino icecube-170922a. *Science*, 361.

[32] FA Aharonian. Tev gamma rays from bl lac objects due to synchrotron radiation of extremely high energy protons. *New Astronomy*, 5(7):377–395, 2000.

[33] Karl Mannheim. The proton blazar. *Astronomy and Astrophysics*, 269:67–76, 1993.

[34] A Mücke and RJ Protheroe. A proton synchrotron blazar model for flaring in markarian 501. *Astroparticle Physics*, 15(1):121–136, 2001.

[35] M Cerruti, A Zech, C Boisson, and S Inoue. A hadronic origin for ultra-high-frequency-peaked bl lac objects. *Monthly Notices of the Royal Astronomical Society*, 448(1):910–927, 2015.

[36] Charles R Harris, K Jarrod Millman, Stéfan J Van Der Walt, Ralf Gommers, Pauli Virtanen, David Cournapeau, Eric Wieser, Julian Taylor, Sebastian Berg, Nathaniel J Smith, et al. Array programming with numpy. *Nature*, 585(7825):357–362, 2020.

[37] Pauli Virtanen, Ralf Gommers, Travis E Oliphant, Matt Haberland, Tyler Reddy, David Cournapeau, Evgeni Burovski, Pearu Peterson, Warren Weckesser, Jonathan Bright, et al. Scipy 1.0: fundamental algorithms for scientific computing in python. *Nature methods*, 17(3):261–272, 2020.

[38] Adrian M Price-Whelan, BM Sipőcz, HM Günther, PL Lim, SM Crawford, S Conseil, DL Shupe, MW Craig, N Dencheva, A Ginsburg, et al. The astropy project: building an open-science project and status of the v2. 0 core package. *The Astronomical Journal*, 156(3):123, 2018.

[39] Thomas P Robitaille, Erik J Tollerud, Perry Greenfield, Michael Droettboom, Erik Bray, Tom Aldcroft, Matt Davis, Adam Ginsburg, Adrian M Price-Whelan, Wolfgang E Kerzendorf, et al. Astropy: A community python package for astronomy. *Astronomy & Astrophysics*, 558:A33, 2013.

[40] Víctor Zabalza. naima: a python package for inference of relativistic particle energy distributions from observed nonthermal spectra. *arXiv preprint arXiv:1509.03319*, 2015.

[41] Andrea Tramacere. Jetset: Numerical modeling and sed fitting tool for relativistic jets. *Astrophysics Source Code Library*, pages ascl–2009, 2020.

[42] C Nigro, J Sitarek, P Gliwny, D Sanchez, A Tramacere, and M Craig. agnpy: An open-source python package modelling the radiative processes of jetted active galactic nuclei. *Astronomy & Astrophysics*, 660:A18, 2022.

[43] Christoph Deil, Roberta Zanin, Julien Lefaucheur, Catherine Boisson, Bruno Khélifi, Régis Terrier, Matthew Wood, Lars Mohrmann, Nachiketa Chakraborty, Jason Watson, et al. Gammapy-a prototype for the cta science tools. *arXiv preprint arXiv:1709.01751*, 2017.

[44] Justin D Finke, Charles D Dermer, and Markus Böttcher. Synchrotron self-compton analysis of tev x-ray-selected bl lacertae objects. *The Astrophysical Journal*, 686(1):181, 2008.

[45] Ni I Shakura and Rashid Alievich Sunyaev. Black holes in binary systems. observational appearance. *Astronomy and Astrophysics*, 24:337–355, 1973.

[46] Charles D Dermer and Reinhard Schlickeiser. Transformation properties of external radiation fields, energy-loss rates and scattered spectra, and a model for blazar variability. *The astrophysical journal*, 575(2):667, 2002.

[47] Charles D Dermer, Justin D Finke, Hannah Krug, and Markus Böttcher. Gamma-ray studies of blazars: Synchro-compton analysis of flat spectrum radio quasars. *The Astrophysical Journal*, 692(1):32, 2009.

[48] Justin D Finke. External compton scattering in blazar jets and the location of the gamma-ray emitting region. *The Astrophysical Journal*, 830(2):94, 2016.

[49] George R Blumenthal and Robert J Gould. Bremsstrahlung, synchrotron radiation, and compton scattering of high-energy electrons traversing dilute gases. *Reviews of modern Physics*, 42(2):237, 1970.

[50] A Crusius and R Schlickeiser. Synchrotron radiation in random magnetic fields. *Astronomy and Astrophysics*, 164:L16–L18, 1986.

[51] FA Aharonian, SR Kelner, and A Yu Prosekin. Angular, spectral, and time distributions of highest energy protons and associated secondary gamma rays and neutrinos propagating through extragalactic magnetic and radiation fields. *Physical Review D*, 82(4):043002, 2010.

[52] RJ Gould. Compton and synchrotron processes in spherically-symmetric non-thermal sources. *Astronomy and Astrophysics*, 76:306–311, 1979.

[53] M Georganopoulos, JG Kirk, and A Mastichiadis. The beaming pattern and spectrum of radiation from inverse compton scattering in blazars. *The Astrophysical Journal*, 561(1):111, 2001.

[54] Frank C Jones. Calculated spectrum of inverse-compton-scattered photons. *Physical Review*, 167(5):1159, 1968.

[55] Robert J Gould. *Electromagnetic processes*, volume 11. Princeton University Press, 2006.

[56] JM Jauch, F Rohrlich, JM Jauch, and F Rohrlich. External field problems. *The Theory of Photons and Electrons: The Relativistic Quantum Field Theory of Charged Particles with Spin One-half*, pages 327–389, 1976.

[57] Robert J Gould and Gérard P Schréder. Pair production in photon-photon collisions. *Physical Review*, 155(5):1404, 1967.

[58] Anita Mücke, Ralph Engel, Jörg P Rachen, Raymond J Protheroe, and Todor Stanev. Monte carlo simulations of photohadronic processes in astrophysics. *Computer Physics Communications*, 124(2-3):290–314, 2000.

[59] A Mücke, RJ Protheroe, R Engel, JP Rachen, and T Stanev. Bl lac objects in the synchrotron proton blazar model. *Astroparticle Physics*, 18(6):593–613, 2003.

[60] Direct neutrino-mass measurement with sub-electronvolt sensitivity. *Nature Physics*, 18(2):160–166, 2022.